Numerical Simulation of Hydrodynamic Bearings with Engineered Slip/No-Slip Surfaces

A Thesis

Presented to

The Academic Faculty

By

Alicia Fortier

In Partial Fulfillment

of the Requirements for the Degree

Masters of Science in Mechanical Engineering

Georgia Institute of Technology

July 2004

Numerical Simulation of Hydrodynamic Bearings with Engineered Slip/No-Slip Surfaces

Approved by:

Dr. Richard Salant, Advisor

Dr. Jeffrey Streator

Dr. Steven Danyluk

July 30, 2004

ACKNOWLEDGEMENT

I wish to thank my advisor Dr. Richard Salant for his infinite patience in guiding me through the work for this thesis. I also thank my committee members Dr. Streator and Dr. Danyluk for the time they took to review this thesis as well as the suggestions they had for improvement.

This work was made possible by the support of Georgia Power Company.

TABLE OF CONTENTS

LIST OF TABLES

LIST OF FIGURES

LIST OF SYMBOLS

A	dimensionless slip coefficient, equations (19) and (36)
a	coefficients defined by equations (60), (61) and (65)
B	variable defined by equation (63)
c	clearance, equation (25)
C	variable defined by equation (59)
D	dimensionless recess depth, d/h_o
e	eccentricity
E	east nodal point
ε	eccentricity ratio, e/c
F	cavitation index defined by equations (32)-(34)
$\hat{F}$	dimensionless friction force, equations (24)
F^*	dimensionless friction force, equation (50)
F_f	friction force, equation (17), (49)
f	friction coefficient, W/F_f
h	film thickness, equation (1), (25)
h_i	film thickness at X=1
h_o	film thickness at X=0
H	dimensionless film thickness, equations (19) and (36)

H_i	H at X=0
K	variable defined by equation (58)
k	variable defined by equation (61)
L	aspect ratio, L_x/L_y
ℓ	dimensionless length of slip or recess Region I
L_s	length of slip or recess Region I
L_x	length of bearing in x direction
L_y	length of bearing in y direction
N	rotational speed of moving surface, rev/s
p	pressure
$\hat{P}$	dimensionless pressure, equations (19) and (36)
P^*	dimensionless pressure equation (37)
p_a	atmospheric pressure
p_c	cavitation pressure
Q	dimensionless side leakage rate, equation (48)
q_x	volumetric flow rate in x direction per unit length in y direction
Q_x	dimensionless volumetric flow rate in x direction per unit length in y direction
q_y	volumetric flow rate in y direction per unit length in x direction
Q_y	dimensionless volumetric flow rate in y direction per unit length in x direction equations (22), (46)
R	journal bearing radius
S	Sommerfeld number, equation (42)
Sc	variable defined in equation (61), (62), (65)

S_p	variable defined in equation (65)
T	dimensionless critical shear stress, equation (55)
T_x	dimensionless shear stress in x direction at z=h , equation (23)
T_y	dimensionless shear stress in y direction at z=h
U	dimensionless speed, equation (19)
u_s	speed of moving surface
u_x	X component of velocity
u_y	Y component of velocity
u_θ	circumferential component of velocity
W	load carrying Capacity, equations (15), and (40)
$\hat{W}$	dimensionless load carrying capacity, equation (21)
W^*	dimensionless load carrying capacity, equation (41)
w	dimensionless width of slip or recess Region I
W_s	width of slip or recess Region I
X	dimensionless x coordinate, x/L_x
Y	dimensionless y coordinate, y/L_y
z	cross film or axial coordinate (Figure 1)
α	slip coefficient, equation (2)
β	angle of action for applied force measured in the clockwise direction, see Figure 2
ϕ	dimensionless pressure in the liquid film region partial film content in cavitation zone, equations 35 and 36
γ	dimensionless speed, equation (36)
μ	viscosity

ρ	average density of two phase cavitated fluid
ρ_c	density of liquid lubricant film
τ_c	critical shear stress value
τ_x	shear stress in x-direction at z=h
τ_y	shear stress in y-direction at z=h
ω	angular speed, rad/s

Subscripts

e	east boundary surface of control volume
E	east nodal point
n	north boundary surface of control volume
N	north nodal point
s	south boundary surface of control volume
P	point of interest
S	south nodal point
w	west boundary surface of control volume
W	west nodal point
x^*	coordinate denoting the direction perpendicular to line of centers (Figure 2)
y^*	Coordinate denoting the direction parallel to the line of centers (Figure 2)

SUMMARY

The no-slip boundary condition is the foundation of traditional lubrication theory. It says that fluid adjacent to a solid boundary has zero velocity relative to that solid surface. For most practical applications the no-slip boundary condition is a good model for predicting fluid behavior. However, recent experimental research has found that for special engineered surfaces the no-slip boundary condition is not applicable. Measured velocity profiles suggest that slip is occurring at the interface. In the present study, it is found that judicious application of slip to a bearing's surface can lead to improved bearing performance.

The focus of this thesis is to analyze the effect an engineered slip/no-slip surface could have on hydrodynamic bearing performance. A heterogeneous pattern is applied to the bearing surface in which slip occurs in certain regions and is absent in others. Analysis is performed numerically for both plane pad slider bearings and journal bearings. The performance parameters evaluated for the bearings are load carrying capacity, side leakage rate and friction force. Fluid slip is assumed to occur according to the Navier relation and the effect of a critical value for slip onset is considered.

CHAPTER 1

INTRODUCTION

The assumptions that form the foundations of classical engineering disciplines are frequently taken for granted. In this thesis, the implications of relaxing one of the most fundamental assumptions in fluid dynamics, the no-slip boundary condition, are examined.

Fluid Mechanics plays a major role in the area of Tribology. Specifically, it is the discipline that allows tribologists to examine the role of lubrication. The hydrodynamic bearing, a fundamental machine component, relies on the behavior of the lubricant contained in it to perform its task. The movement of fluid into an entraining gap creates a pressure distribution that allows the bearing to support a load while eliminating contact between solid surfaces. The characteristics of the bearing, which dictate its use, have historically been computed by utilizing the no-slip boundary condition. The question that is addressed in this study is how bearing performance changes if, instead slip is imposed.

This question is answered through numerical modeling. The underlying assumptions of the models being; fluid slip is possible and it is applicable on the scale and in the environment that hydrodynamic bearings demand.

The impetus driving this research is the recent development of surfaces that produce apparent slip with Newtonian fluids. There is a much wider discussion going on about

the fundamental physics of fluids and their interactions with surfaces. It is hoped that this research will supplement that discussion and provide benchmarks for developing technology.

If slip surfaces prove feasible there is great potential for their application in bearings, since it is believed they can reduce energy losses and increase load carrying capacity.

CHAPTER 2

BACKGROUND

The Slip Boundary Condition

Today's models for fluid dynamics were born out of the great enthusiasm for mathematics in the 18th century. Most of the work at that time was focused on perfect fluid flows that are now studied as potential flows. While quite useful, these models fell short in predicting fluid behavior for a great many practical situations. The primary weakness of the idealized models was their inability to explain viscous effects. The search for a more accurate model was the genesis for the controversy that wages on today.

The primary question still as yet not fully answered is:
what happens at the contacting surface between a fluid and a solid boundary?

Today it is usually taught that the fluid at the boundary has zero velocity relative to the solid surface. What is not so often discussed is the controversy that surrounds this theory. The early years of the debate were chronicled by Goldstein (1943) and the results of the debate are presented here.

Three major theories came out of the 19th century over fluid behavior at a solid surface. The first theory, accepted by Coulomb, asserted that the velocity of the fluid at the solid

wall was the same as that of the wall itself and changed continuously through the fluid. The second theory, credited to Girard, said that a thin layer of fluid next to the solid wall stayed completely attached to the wall and that adjacent fluid slipped over the thin layer. He also proposed that the thickness of the attached layer depended on the properties of the system including the temperature, geometry of the solid surface and materials. The third theory, known as the Navier theory, stated that slip did occur on the solid wall and the resulting relative velocity at the interface was proportional to the tangential stress on the solid wall.

A final comprehensive theory about what occurs on the microscopic scale was never adopted. Instead experimental evidence governed what would be used. It was found that for most practical cases, whether slip occurred or not, the effect on the macroscopic flow field was small and the no slip boundary condition gave good results for predicting fluid behavior.

There have always existed exceptions to the no-slip rule. An early example is the research Maxwell did on rarefied gases. He concluded that these gases exhibited considerable slip at solid boundaries.

Modern Applications

The debate is once again being pushed to the forefront because of developing technologies that require an understanding of fluid behavior at the interface. Slip, first widely researched in polymer melts (Meigler, Hervet and Leger 1993; Horn, et al. 2000), is now re-emerging as an intense field of research due to the advances in micro and

nano scale technology. It has been found that slip is an important factor at these small scales. This makes slip an important tribological consideration for micro machine technology and research has been specifically directed at this area (Meyer, et al. 1998; Reiter, et al. 1994; Riedo, Levy and Brune 2002).

Application of slip may not be restricted to the small in scale. Some developments in surface technologies show promise for wider use. These surfaces must be non-wetting and fall into two classes. The first are molecularly smooth surfaces like mica. The second are surfaces with micron scale patterns (Pit, Hervet and Leger 2000; Baudry and Charlaix 2001; Hasegawa, et al. 1999).

The important aspect of these surfaces, from the perspective of a numerical simulation, is choosing a model for the slip boundary condition. Two works of experimental research guided the choice for this analysis.

In 1999, Keizo Wantanabe, Yanuar and Hirosi Udagaw published their experimental study of flow through a pipe with highly water repellant walls. The pipe measured 16 mm in diameter and had a highly water repellent coating applied to it. Using tap water they found that they achieved a 14% reduction in drag. They also found that the slip velocity, extrapolated from measurements of the macroscopic flow field, was directly proportional to the shear stress.

In 2001, Yingxi Zhu and Steve Granick from the University of Illinois, Urbana published their experimental research on rate dependent slip for molecularly smooth surfaces. In this study a drop of Newtonian liquid was placed between two partially wetting smooth

surfaces whose spacing was vibrated. The hydrodynamic forces were measured and compared to those predicted by the no-slip boundary condition. They found good agreement with the no-slip condition at low speeds. Above a critical level, however, the results deviated from the prediction. Hydrodynamic forces for higher speeds "became up to 2-4 orders of magnitude less than expected by assuming the no-slip boundary condition," implying partial slip.

In 2003 Hugh Spikes collaborated with Granick to develop a mathematical model for slip based on the experimental work (Spikes and Granick 2003). Additionally, Spikes analyzed the potential application of the slip surfaces on hydrodynamic lubrication (Spikes 2003 a., 2003b.). The bearing used in the analysis was a plane pad slider bearing with a homogeneous slip surface. The focus of the analysis was the effect of critical shear stress on load support and frictional losses as well as the feasibility of slip surfaces in low load contacts.

Thus far, experimental works on slip surfaces suggest the Navier boundary condition as a strong contender for modeling slip. Zhu and Granick additionally suggested a critical value of shear stress may need to be attained before slip onset. In the development of the model for this thesis, both boundary conditions are considered.

CHAPTER 3

METHODS

3.1 Problem Formulation

Case I- Slider Bearing with Navier Slip Condition
(Salant and Fortier 2004)

Bearing Configuration

The bearing examined in Case I is the simple inclined pad bearing. In this bearing the film thickness, or the height of the fluid film separating the two surfaces, is a linear function of x (Equation (1)). The top surface, labeled as Surface 2 in Figure 1a. is stationary while the bottom surface, Surface 1, is moving at a driving speed u_s. Due to the direction of the driving velocity the fluid is pulled into the bearing at the maximum film thickness, h_i, and proceeds through a converging wedge resulting in hydrodynamic pressure generation.

$$h(x) = h_i - \frac{(h_i - h_0)}{L_x} x \tag{1}$$

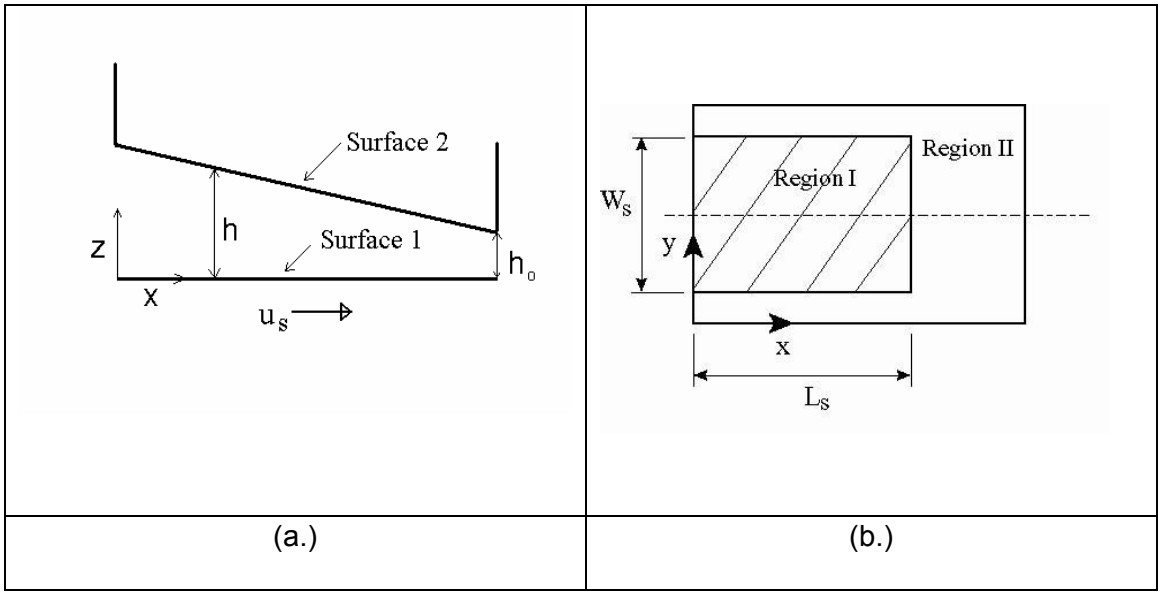

Figure 1- (a.) Diagram of a plane pad slider bearing as seen from the side (b.) Slip/no-Slip pattern applied to Surface 2

A slip/no-slip pattern, shown in Figure 1b., is applied to the stationary Surface 2. A rectangular area is selected for application of slip. This area, considered the slip pad, is centered with respect to the y dimension and is placed flush with the fluid inlet edge. It is surrounded on the three remaining sided by the no-slip Region II. The desired effect is for the fluid to first flow through the slip region and then exit through the no-slip region.

Boundary Conditions

In Case I, slip is modeled by the Navier condition, which says that the slip velocity is directly proportional to the shear stress at the fluid-solid interface. According to the bearing configuration, Surface 1 is no-slip everywhere while Surface 2 will have one

region with slip and another region without. For x locations that fall within the slip region the boundary conditions are:

$$\begin{aligned} z = 0 \quad , \qquad & u_x = u_s , \quad u_y = 0 \\ z = h \quad , \qquad & u_x = -\alpha\mu \frac{\partial u_x}{\partial z}, \quad u_y = -\alpha\mu \frac{\partial u_y}{\partial z} \end{aligned} \tag{2}$$

The proportionality constant α is non-negative and will be referred to as the slip coefficient. If the slip coefficient is set equal to zero the above boundary condition reduces to the conventional no-slip case. Therefore, this boundary condition is applicable to x locations that fall within the no-slip region as well as the slip region. The only difference from a modeling perspective being the value assigned to α.

Governing Equation

With the boundary conditions established, formulation of the governing equation begins. A number of assumptions are made to simplify the model.

1. Body forces are neglected
2. The pressure is constant across the film thickness (in the z direction)
3. The fluid is Newtonian
4. Flow is laminar
5. Inertial forces are neglected
6. Viscosity is constant

Applying these assumptions to the Navier-Stokes relations in two dimensions gives a starting point for describing the fluid system.

$$\frac{\partial^2 u_x}{\partial z^2} = \frac{1}{\mu}\frac{\partial p}{\partial x} \tag{3}$$

$$\frac{\partial^2 u_y}{\partial z^2} = \frac{1}{\mu}\frac{\partial p}{\partial y} \tag{4}$$

Combining Equations (3) and (4) with the boundary conditions in Equation (2) results in a boundary value problem that is solved analytically to obtain equations for velocity in both the x and y directions.

The first step in this solution is to integrate the Navier Stokes component twice with respect to z giving the general form of the velocity equation. The boundary conditions are then used to find the constants of integration.

$$u_x = \frac{1}{2\mu}\frac{\partial p}{\partial x} z^2 + C_1 z + C_2 \tag{5}$$

$$u_x(z=0) = u_s = C_2 \tag{6}$$

$$u_x(z=h) = -\alpha\mu\frac{\partial u_x}{\partial z} = \frac{1}{2\mu}\frac{\partial p}{\partial x}h^2 + C_1 h + u_s \tag{7}$$

$$C_1 = -\frac{h}{2\mu}\frac{\partial p}{\partial x}\left\{\frac{h+2\alpha\mu}{h+\alpha\mu}\right\} - \frac{u_s}{h+\alpha\mu} \tag{8}$$

Substituting the coefficients yields the full expression for velocity.

$$u_x = \frac{1}{2\mu}\frac{\partial p}{\partial x}z^2 - \frac{h}{2\mu}\frac{\partial p}{\partial x}\left\{\frac{h+2\alpha\mu}{h+\alpha\mu}\right\}z - \frac{u_s}{h+\alpha\mu}z + u_s \tag{9}$$

The solution for u_y is very similar. The only difference being, the value C_2 is zero because there is no driving velocity in the y direction.

$$u_y = \frac{1}{2\mu}\frac{\partial p}{\partial y}z^2 - \frac{h}{2\mu}\frac{\partial p}{\partial y}\left\{\frac{h+2\alpha\mu}{h+\alpha\mu}\right\}z \tag{10}$$

These velocities are used to compute the flow rates in each direction. When input into the continuity equation a modified Reynolds equation results.

$$\frac{\partial q_x}{\partial x} + \frac{\partial q_y}{\partial y} = 0 \tag{11}$$

$$q_x = \int_0^h u_x \, dz = -\frac{h^3}{12\mu}\frac{\partial p}{\partial x}\left\{1 + \frac{3\alpha\mu}{h+\alpha\mu}\right\} + \frac{u_s h}{2}\left\{1 + \frac{\alpha\mu}{h+\alpha\mu}\right\} \tag{12}$$

$$q_y = \int_0^h u_y \, dz = -\frac{h^3}{12\mu}\frac{\partial p}{\partial y}\left\{1 + \frac{3\alpha\mu}{h+\alpha\mu}\right\} \tag{13}$$

$$\frac{\partial}{\partial x}\left\{\frac{h^3}{12\mu}\frac{\partial p}{\partial x}\left(1 + \frac{3\alpha\mu}{h+\alpha\mu}\right)\right\} + \frac{\partial}{\partial y}\left\{\frac{h^3}{12\mu}\frac{\partial p}{\partial y}\left(1 + \frac{3\alpha\mu}{h+\alpha\mu}\right)\right\} = \frac{\partial}{\partial x}\left\{\frac{u_s h}{2}\left(1 + \frac{\alpha\mu}{h+\alpha\mu}\right)\right\} \tag{14}$$

This modified Reynolds equation (14) is the governing equation for the fluid lubrication system. Note that if the slip coefficient, α, is set to zero, Equation (14) reduces to the standard Reynolds equation (Hamrock 1994).

Performance Parameters

There are a number of performance parameters that are examined for the plane pad bearing. The first is the bearing load carrying capacity. The load carrying capacity is defined as the integral of the pressure profile over the bearing area and is the total load the bearing can support for the given film thickness distribution.

$$W = \int_0^{L_y} \int_0^{L_x} p(x,y)dxdy \tag{15}$$

Another important parameter is the flow rate of fluid exiting the bearing, perpendicular to the direction of the driving velocity. For this bearing configuration it corresponds to fluid flowing outward from the centerline in the $\pm y$ direction. The flow rate is calculated by integrating the fluid velocity at the side edges of the bearing over the film thickness.

$$q_y = \int_0^h u_y\Big|_{y=L_y} dz = -\frac{h^3}{6\mu}\frac{\partial p}{\partial y}\left\{1 + \frac{3\alpha\mu}{h+\alpha\mu}\right\} \tag{16}$$

The friction force generated by the lubrication system is due to the fluid viscous forces and is a very important parameter for evaluating bearing losses. It is calculated by integrating interface shear stress over the interface surface area.

$$F_f = \int_0^{L_y} \int_0^{L_x} \tau_x(x,y)\, dxdy \tag{17}$$

$$\tau_x(x,y) = \mu \frac{\partial u_x}{\partial z}\bigg|_{z=h} \tag{18}$$

Non-Dimensional Equations

Non-dimensional forms of the governing equations and performance parameters are used in the numerical model.

$$H = \frac{h}{h_0} \qquad X = \frac{x}{L_x} \qquad Y = \frac{y}{L_y} \qquad \hat{P} = \frac{p}{p_a} \qquad A = \frac{\alpha\mu}{h_0}$$
$$L = \frac{L_x}{L_y} \qquad U = \frac{6u_s\mu L_x}{p_a h_0^2} \tag{19}$$

Reynolds Equation:

$$\frac{\partial}{\partial X}\left\{H^3\frac{\partial \hat{P}}{\partial X}\left(1+\frac{3A}{H+A}\right)\right\}+L^2\frac{\partial}{\partial Y}\left\{H^3\frac{\partial \hat{P}}{\partial Y}\left(1+\frac{3A}{H+A}\right)\right\}=U\frac{\partial}{\partial X}\left\{H\left(1+\frac{A}{H+A}\right)\right\} \tag{20}$$

The calculation of performance parameters is done with the results of the numerical solution for pressure. The program solves and outputs based on the dimensionless form of the modified Reynolds equation; it is therefore, advantageous to formulate the performance parameters based on the dimensionless quantities.

The integral for load carrying capacity, Equation (15), in terms of dimensionless quantities becomes,

$$\hat{W} = \frac{W}{p_a L_x L_y} = \int_0^1\int_0^1 \hat{P}(X,Y)\,dXdY \tag{21}$$

and Equation (16), becomes,

$$Q_y = -H^3 \frac{\partial \hat{P}}{\partial Y}\left\{1+\frac{3A}{H+A}\right\} = \frac{6\mu L_y}{h_0{}^3 p_a} q_y \tag{22}$$

In the case of the friction force a dimensionless shear stress must be found. It is then integrated to give the final dimensionless friction force.

$$T_x(X,Y) = \left[H \frac{\partial \hat{P}}{\partial x}\left\{\frac{H}{H+A}\right\} - \frac{U}{3}\left\{\frac{1}{H+A}\right\}\right] \tag{23}$$

$$\hat{F} = \int_0^1 \int_0^1 T_x(X,Y)\, dXdY = \frac{2\mu}{h_o p_a L_y} F_f \tag{24}$$

Case II- Journal Bearing with Navier Slip Condition

Bearing Configuration

In Case II the journal bearing is examined. The journal bearing consists of a circular shaft rotating inside a circular sleeve. As shown in Figure 2, the diameter of the sleeve is slightly larger than that of the shaft allowing for the addition of fluid lubricant to the system.

The difference in the radius of the sleeve and shaft is the bearing clearance, c. Under operating conditions the shaft's equilibrium position is not concentric with the sleeve but offset from the sleeve's center by a distance referred to as the eccentricity, e. A line drawn through the sleeve center and shaft center passes through the point of minimum film thickness and is called the line of centers. This line is shown in Figure 2.

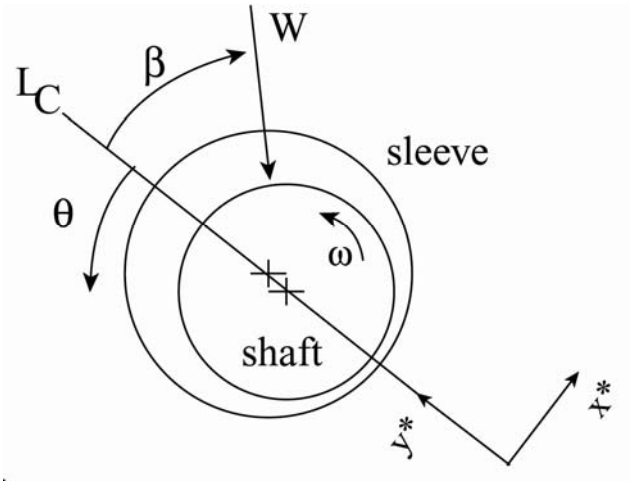

Figure 2- Diagram of journal bearing configuration

The thickness of the lubricant film is a function of the bearing clearance, eccentricity and θ location, as seen in Equation (25). The θ axis originates and ends at the line of centers where the film thickness is maximum. Minimum film thickness occurs at θ equal to π.

$$h(\theta) = c + e\cos(\theta) \tag{25}$$

With the film thickness defined, a model is created which transfers the bearing configuration to a Cartesian format. The bearing is considered to be 'cut' at the line of centers, where θ equals zero, and opened such that the film thickness is retained as a function of θ. The problem can then be more simply analyzed with respect to a Cartesian coordinate system of θ, y and z as shown in Figure 3 (a.)

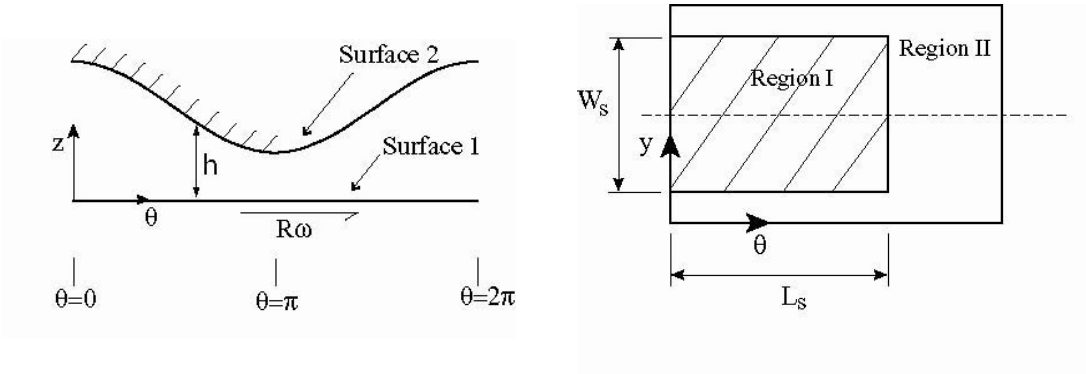

(a.) (b.)

Figure 3- (a.) Diagram of journal bearing in Cartesian coordinate configuration, (b.) Diagram of surface pattern applied to Surface 2.

The bottom surface in Figure 3 (a.) represents the shaft and moves at speed u_s equal to the bearing radius times the angular velocity. The slip/no-slip surface is applied to the stationary surface of the bearing sleeve, Surface 2. The shape and orientation of the slip region is similar to that described in the case of the plane pad bearing as shown in Figure 3 (b.)

Boundary Conditions

As in Case I the slip is modeled with the Navier condition. This boundary condition is written explicitly in Equation (26).

$$z = 0 \quad , \qquad u_\theta = u_s , \quad u_y = 0$$
$$z = h \quad , \qquad u_\theta = -\alpha\mu \frac{\partial u_\theta}{\partial z}, \quad u_y = -\alpha\mu \frac{\partial u_y}{\partial z} \tag{26}$$

where α is non-zero in Region I and zero in Region II.

An additional boundary condition used in Case II, is that imposed by the lubricant inlet. In this study, a solution technique is used that depends on continuity of flow or mass conservation. Therefore, lubricant must be continuously supplied to the bearing in order to account for the lubricant lost through side leakage. This ensures that the bearing is not starved and therefore is able to maintain the prescribed film thickness. In this model the pressure is specified as atmospheric at $\theta = 0$ to simulate fluid inlet at that location.

$$p\big|_{\theta=0} = p_a \tag{27}$$

Governing Equation

The assumptions used in the derivation of the governing equations for the journal bearing are the same as those used for the plane pad bearing. The resulting modified Reynolds equation for Case II (Equation (28)) is found by transforming the x coordinate to θ and putting u_s into its angular form $R\omega$.

$$x \Rightarrow R\theta \qquad u_s \Rightarrow R\omega$$

Modified Reynolds Equation of Journal Bearing:

$$\frac{1}{R^2}\frac{\partial}{\partial\theta}\left\{\frac{h^3}{12\mu}\frac{\partial p}{\partial\theta}\left(1+\frac{3\alpha\mu}{h+\alpha\mu}\right)\right\}+\frac{\partial}{\partial y}\left\{\frac{h^3}{12\mu}\frac{\partial p}{\partial y}\left(1+\frac{3\alpha\mu}{h+\alpha\mu}\right)\right\}=\frac{\partial}{\partial\theta}\left\{\frac{(\omega)h}{2}\left(1+\frac{\alpha\mu}{h+\alpha\mu}\right)\right\} \tag{28}$$

The corresponding velocity equations are:

$$u_\theta=\frac{1}{2\mu R}\frac{\partial p}{\partial\theta}z^2-\frac{h}{2\mu R}\frac{\partial p}{\partial\theta}\left\{\frac{h+2\alpha\mu}{h+\alpha\mu}\right\}z-\frac{R\omega}{h+\alpha\mu}z+R\omega \tag{29}$$

$$u_y=\frac{1}{2\mu}\frac{\partial p}{\partial y}z^2-\frac{h}{2\mu}\frac{\partial p}{\partial y}\left\{\frac{h+2\alpha\mu}{h+\alpha\mu}\right\}z \tag{30}$$

Cavitation Model and Dimensionless Reynolds Equations

An important consideration in the model for the journal bearing is cavitation of the lubricant film. The bearing's converging-diverging film thickness profile creates two distinct regions. In the converging section of the bearing the lubricant is acting under a compressive force. The lubricant responds by generating positive pressure to separate the surfaces. In the diverging section tensile forces are applied to the lubricant. The liquid film is unable to sustain these forces and ruptures. Within this cavitation region, the lubricant is a two phase mixture.

The challenge in modeling the journal bearing is ensuring that mass is conserved at both film rupture and film reformation. The method used for this analysis was developed by Payvar and Salant (1992) for application in mechanical seals. It is described in detail in their paper and is briefly summarized here.

The governing equation for the full liquid film region is described by Equation (28). The fluid density in this regime is named ρ_c and has been eliminated from the equation because it is a constant value.

For the cavitated zone the pressure is equal to the cavitation pressure and stays constant. The governing equation in this region therefore reduces to Equation (31).

$$0 = \frac{\partial}{\partial \theta}\left\{\frac{\rho}{\rho_c} h\left(1 + \frac{\alpha\mu}{h + \alpha\mu}\right)\right\} \tag{31}$$

The variable ρ in Equation (31) represents the average density of the two phase fluid. In the cavitated zone both liquid and vapor are present making density an important parameter.

These two regimes are united into a single governing equation by the introduction of variables F and ϕ. Such that:

$$\frac{p - p_c}{p_a} = F\phi \tag{32}$$

$$\frac{\rho}{\rho_c} = 1 + (1 - F)\phi \tag{33}$$

Where:

$$\begin{aligned} F(\theta, y) &= 0 \qquad if \quad \phi \le 0 \\ F(\theta, y) &= 1 \qquad if \quad \phi > 0 \end{aligned} \tag{34}$$

New variable F is the cavitation index. It assumes values of one and zero in the full liquid film and cavitation regions respectively. The index serves to change the meaning of ϕ in the two regions. In the liquid film region ϕ is a dimensionless pressure as seen in Equation (32). In the cavitated region, however, ϕ is an indicator of the relative densities or partial film content (Equation (33)).

Equation (35) shows the dimensionless modified Reynolds equation. The variables F and ϕ have been substituted so that the single equation governs both the full liquid film and cavitation regions. Note that setting F equal to zero eliminates the entire left hand side of the equation, leaving the dimensionless form of Equation (31). If F is instead set to one, the right hand side reduces leaving the dimensionless form of Equation (28).

Dimensionless Reynolds Equation:

$$\frac{\partial}{\partial\theta}\left\{H^3\frac{\partial(F\phi)}{\partial\theta}\left(1+\frac{3A}{(H+A)}\right)\right\}+\frac{\partial}{\partial Y}\left\{H^3\frac{\partial(F\phi)}{\partial Y}\left(1+\frac{3A}{(H+A)}\right)\right\}=$$
$$\gamma\frac{\partial}{\partial\theta}\left\{H\left(1+(1-F)\phi\right)\left(1+\frac{A}{(H+A)}\right)\right\} \tag{35}$$

The dimensionless quantities are redefined for the journal bearing in terms of different known values from those used in the plane pad bearing. The bearing length is non-dimensionalized by the radius, the film thickness and slip constant are non-dimensionalized with respect to clearance and the new dimensionless quantity γ is introduced.

$$H=\frac{h}{c}\qquad Y=\frac{y}{R}\qquad \hat{P}=\frac{p-p_c}{p_a}=F\phi\qquad A=\frac{\alpha\mu}{c}$$
$$\gamma=\frac{6\omega\mu}{p_a}\left(\frac{R}{c}\right)^2 \tag{36}$$

Performance Parameters

The performance parameters for the journal bearing differ slightly from those for the plane pad bearing. Once again, the objective is to formulate the parameters in terms of dimensionless quantities; this time however, a slight modification is made to the pressure output from the program.

For purposes of calculating load carrying capacity the pressure is modified so that the zero point is moved as to correspond with atmospheric pressure. This gage pressure is referred to as P^*.

$$P^* = \frac{p - p_a}{p_a} = \hat{P} + \frac{p_c - p_a}{p_a} \tag{37}$$

The load carrying capacity is solved in terms of this new pressure. The load can be thought of as the resultant of two load vectors defined with respect to their angular distance from the line of centers, β (Figure 2). Where, β is measured in the clockwise direction.

$$W_{y^*} = p_a R^2 \int_0^{2(L/D)} \int_0^{2\pi} P^* \cos\theta \, d\theta \, dY \tag{38}$$

$$W_{x^*} = p_a R^2 \int_0^{2(L/D)} \int_0^{2\pi} P^* \cos\theta \, d\theta \, dY \tag{39}$$

$$W = \sqrt{(W_{x^*})^2 + (W_{y^*})^2} = p_a R^2 W^* \tag{40}$$

$$W^* = \sqrt{\left[\int_0^{2(L/D)} \int_0^{2\pi} P^* \cos\theta \, d\theta \, dY\right]^2 + \left[\int_0^{2(L/D)} \int_0^{2\pi} P^* \sin\theta \, d\theta \, dY\right]^2} \tag{41}$$

A more commonly used quantity to describe the load characteristics of a journal bearing is the Sommerfeld number. The Sommerfeld number is dimensionless and is inversely related to the load carrying capacity as Equation (44) shows.

The definition of the Sommerfeld number is:

$$S = \frac{\mu N}{p_{rep}} \left(\frac{R}{c} \right)^2 \tag{42}$$

Where p_{rep} is a representative pressure, calculated by dividing the load by the projected area, and N is the rotational speed in revolutions per second.

$$p_{rep} = \frac{W}{L_y D} = \frac{W^* p_a R}{2 L_y}, \quad N = \frac{\omega}{2\pi} \tag{43}$$

The Sommerfeld number can be written in terms of the dimensionless load and speed, W^* and γ as:

$$S = \frac{\gamma}{3\pi} \left(\frac{L_y}{D} \right) \frac{1}{W^*} \tag{44}$$

The flow rate exiting the side of the bearing is calculated in a manner similar to that of Case I. Equation (46) is the dimensionless side leakage rate for the journal bearing as found using the previously described method.

$$q_y = -\frac{c^3 p_a}{R^2}\rho_c\left[H^3\frac{\partial P^*}{\partial Y}\left\{1+\frac{3A}{H+A}\right\}\right] \tag{45}$$

$$Q_y = -\left[H^3\frac{\partial P^*}{\partial Y}\left\{1+\frac{3A}{H+A}\right\}\right] = \frac{R^2}{c^3 p_a \rho_c} q_y \tag{46}$$

Another common way of representing side leakage rate is to non-dimensionalize it in relation to the flow rate in the circumferential direction as in Equation (48).

$$q_\theta = -\frac{c^3 p_a}{R^2}\rho_c\left[H^3\frac{\partial P^*}{\partial \theta}\left\{1+\frac{3A}{H+A}\right\}+\gamma\frac{\partial}{\partial \theta}\left\{\frac{\rho}{\rho_c}H\right\}\right] \tag{47}$$

$$Q = \frac{q_y}{q_\theta} \tag{48}$$

Once again the friction force is found in a manner similar to Case I. The dimensionless form of the friction force is given by Equation (50).

$$F_f = \frac{cR\ p_a}{2}\int_0^{2(L/D)}\int_0^{2\pi}\left[H\frac{\partial P^*}{\partial x}\left\{\frac{H}{H+A}\right\}-\frac{\gamma}{3}\left\{\frac{1}{H+A}\right\}\right]d\theta\, dY \tag{49}$$

$$F^* = \frac{2}{cR\ p_a}F_f = \int_0^{2(L/D)}\int_0^{2\pi}\left[H\frac{\partial P^*}{\partial x}\left\{\frac{H}{H+A}\right\}-\frac{\gamma}{3}\left\{\frac{1}{H+A}\right\}\right]d\theta\, dY \tag{50}$$

For the journal bearing an additional descriptor is used for the friction characteristics. It is the friction coefficient multiplied by the ratio of the bearing radius to the clearance. In Equation (51) this quantity is expressed in terms of the dimensionless load carrying capacity and friction force.

$$f\left(\frac{R}{c}\right) = \frac{1}{2}\frac{F^*}{W^*} \tag{51}$$

Case III- Slider Bearing with Critical Shear Stress

In Case III the plane pad bearing is reconsidered. The bearing configuration is the same as that presented in Case I. The objective of Case III is to investigate the effect of a critical onset value for slip as suggested by Zhu and Granick (2001).

Region I applied to the stationary inclined surface is the permissible slip region. Slip will only occur within this region if a critical shear stress, τ_c, is exceeded. The no-slip boundary condition will govern in areas in this region where the critical value is not exceeded as well as in Region II.

Boundary Conditions

The boundary condition for Case III involves the evaluation and comparison of the interface shear stress at Surface 2. If the magnitude of the resultant shear stress vector is greater than the magnitude of the critical shear stress, then slip is said to occur. The resulting slip velocity is directly proportional to the difference between the boundary shear stress and the critical value with a proportionality constant α. The direction of the slip velocity is the same as the resultant shear stress value and may be decomposed into its x and y components as in Equation (52).

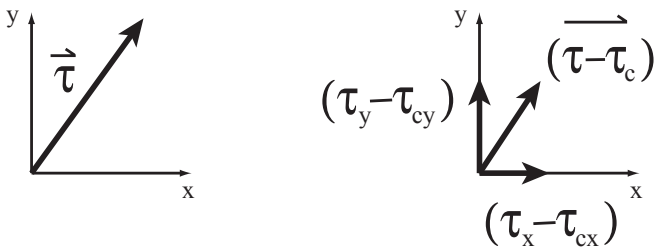

Figure 4- Diagram of resultant shear stress vector and vectors used to determine slip velocity.

$$z = 0 \quad , \qquad u_x = U, \quad u_y = 0$$

$$z = h \quad , \qquad u_x = \begin{cases} 0 & if \ |\vec{\tau}| < \tau_c \\ \alpha(\tau - \tau_c)_x & if \ |\vec{\tau}| < \tau_c \end{cases} \quad , \qquad (52)$$

$$u_y = \begin{cases} 0 & if \ |\vec{\tau}| < \tau_c \\ \alpha(\tau - \tau_c)_y & if \ |\vec{\tau}| < \tau_c \end{cases}$$

If the critical shear stress is not exceeded or if the slip coefficient is equal zero the velocity along Surface 2 reduces to zero. Additionally, if the critical shear stress is equal to zero, the boundary condition reduces to the Navier boundary condition used in Case I.

Governing Equation

The governing equation that results for the critical shear stress boundary condition is developed by the same method used for the Navier condition. The resulting modified Reynolds equation is shown in Equation (53). The last term in the equation has a plus and minus sign due to the symmetry of flow in the y direction. If the *x-y* location lies

below the vertical symmetry line of the bearing ($y<L_y/2$) then the sign is positive. If it is located above the symmetry line, the term is negative.

$$\frac{\partial}{\partial x}\left\{h^3\frac{\partial p}{\partial x}\left(1+\frac{3\alpha\mu}{(h+\alpha\mu)}\right)\right\}+\frac{\partial}{\partial y}\left\{h^3\frac{\partial p}{\partial y}\left(1+\frac{3\alpha\mu}{(h+\alpha\mu)}\right)\right\}$$
$$=6\mu u_s\frac{\partial}{\partial x}\left\{h\left(1+\frac{\alpha\mu}{(h+\alpha\mu)}\right)\right\}-6\tau_c\frac{\partial}{\partial x}\left\{\frac{\alpha h^2}{h+\alpha}\right\}\pm 6\tau_c\frac{\partial}{\partial y}\left\{\frac{\alpha h^2}{h+\alpha}\right\} \quad (53)$$

Equation (53) is the governing equation for location where the interface shear stress exceeds the critical value. If the critical shear stress τ_c is set to zero, Equation (53) reduces to Equation (14), the governing equation for Case I. Alternatively, if the slip coefficient is set to zero the equation reduces to the standard Reynolds equation. In regions where the critical shear stress value is not exceeded the standard Reynolds equation governs.

The dimensionless form of the modified Reynolds equation for Case III is shown in Equation (54). The dimensionless quantities are the same as those used in Equation (19), with one additional quantity for the dimensionless critical shear stress which is defined below in Equation (55).

$$\frac{\partial}{\partial X}\left\{H^3\frac{\partial \hat{P}}{\partial X}\left(1+\frac{3A}{(H+A)}\right)\right\}+L^2\frac{\partial}{\partial Y}\left\{H^3\frac{\partial \hat{P}}{\partial Y}\left(1+\frac{3A}{(H+A)}\right)\right\}$$
$$=U\frac{\partial}{\partial X}\left\{H\left(1+\frac{A}{(H+A)}\right)\right\}-T\frac{\partial}{\partial X}\left\{\frac{AH^2}{(A+H)}\right\}\pm TL\frac{\partial}{\partial Y}\left\{\frac{AH^2}{(A+H)}\right\} \quad (54)$$

$$T=\frac{6\tau_c l_x}{p_a h_0} \quad (55)$$

3.2 Numerical Scheme

The objective of the numerical scheme is to solve for the pressure in the case of the plane pad bearing and ϕ in the case of the journal bearing. The discretization of the solution space, as well as of the governing differential equation, is done using the micro-control volume method described by Patankar (1980).

Discretization of Solution Space

Slider Bearing

The solution space for the plane pad bearing is a rectangular area in the X Y plane. The space is broken up into an N x M mesh of nodes as shown in Figure 5. The nodes in the Y direction being numbered 1 to N and those in the X direction numbered 1 to M. The number of nodes in each direction is chosen such that ΔX and ΔY are equal. For the slider bearing the mesh is generally 40 x 40.

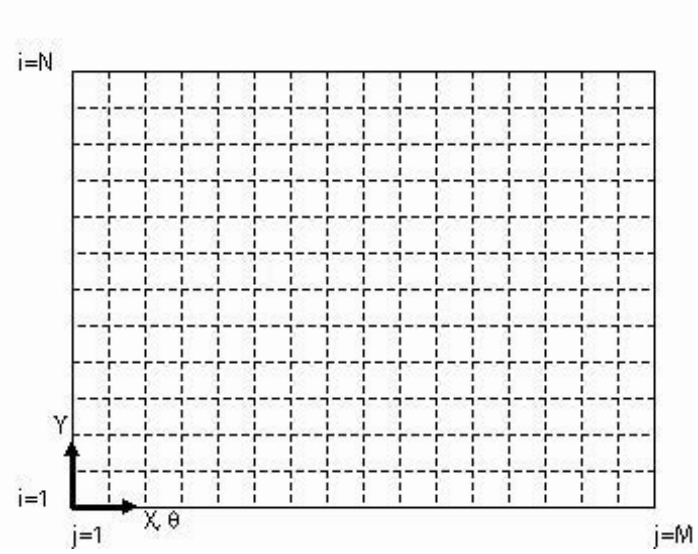

Figure 5- Mesh applied to bearing solution space, intersection point of lines corresponding to position of nodes

Journal Bearing

The solution space for the journal bearing is similar to that for the plane pad bearing. The area is a rectangular area in the $\theta\, y$ plane. The nodes in the Y direction number from 1 to N and those in the θ direction number 1 to M. The number of nodes in each direction is chosen such that ΔY and $\Delta\theta$ are equal and therefore depend on the length to diameter ratio of the bearing.

Boundary Conditions

Slider Bearing

Boundary conditions on the solution space are an important feature to consider when implementing a numerical technique. For the Case I and Case III the pressure is known on all external edges of the bearing because it is open to the atmosphere. In the numerical simulation atmospheric pressure is assigned to all perimeter nodes. The pressure at these nodes remains unchanged throughout the program's execution.

Journal Bearing

For a journal bearing the two edges along the lines $y=0$ and $y=L_y$ open to the atmosphere. The model used for this analysis, however, specifies a fluid inlet at θ equal to 0 (and 2π) which imposes atmospheric pressure at this location. Therefore, as in the plane pad bearing cases, the pressure is atmospheric on the perimeter of the solution space.

Discretization of Governing Equation

Slider Bearing

A control volume formulation is used in discretizing the governing equation. As described by Patankar (1980), the solution space is divided so that each point on the mesh is surrounded by one control volume and that those control volumes are non-overlapping.

Figure 6 illustrates the control volume for node P. It is a rectangular volume whose sides pass through intermediate points n, s, e, w. For this study, the grid spacing is kept uniform and the intermediate points are located half way between the nodes. The resulting control volumes have dimensions ΔX by ΔY.

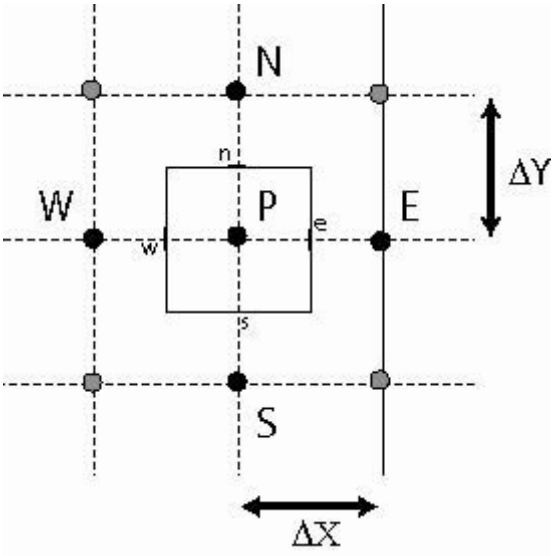

Figure 6- Control volume around node P

The volume is used to solve for the pressure at node P in terms of the pressures at neighboring nodes N, S, E, W. The governing differential equation is integrated over the control volume. This is shown in Equations (56) and (57) for the plane pad bearing of Case I.

$$\int_s^n \int_e^w \frac{\partial}{\partial X}\left\{K\frac{\partial \hat{P}}{\partial X}\right\} dXdY + L^2 \int_s^n \int_e^w \frac{\partial}{\partial Y}\left\{K\frac{\partial \hat{P}}{\partial Y}\right\} dXdY = U\int_s^n \int_e^w \frac{\partial}{\partial X}\{C\} dXdY \tag{56}$$

$$\left\{K\frac{\partial \hat{P}}{\partial X}\right\}_e \Delta Y - \left\{K\frac{\partial \hat{P}}{\partial X}\right\}_w \Delta Y + L^2\left\{K\frac{\partial \hat{P}}{\partial Y}\right\}_n \Delta X - L^2\left\{K\frac{\partial \hat{P}}{\partial Y}\right\}_s \Delta X = U\{C\}_e \Delta Y - U\{C\}_w \Delta Y \tag{57}$$

Where the variables *K* and *C* are substituted to simplify the equation and are defined below.

$$K = H^3\left(1 + \frac{3A}{H + A}\right) \tag{58}$$

$$C = H\left(1 + \frac{A}{H + A}\right) \tag{59}$$

The derivatives are then approximated using a finite difference method.

$$\frac{k_e(P_E - P_P)}{\Delta X}\Delta Y - \frac{k_w(P_P - P_W)}{\Delta X}\Delta Y + \frac{k_n(P_N - P_P)}{\Delta Y}\Delta X - \frac{k_s(P_P - P_S)}{\Delta Y}\Delta X = UC_e\Delta Y - UC_w\Delta Y$$

The final discretized equation is:

$$a_P P_P = a_E P_E + a_W P_W + a_N P_N + a_S P_S + S_c \tag{60}$$

With coefficients:

$$a_E = \frac{k_e}{\Delta X}\Delta Y \qquad k_e = \frac{2K_E K_P}{K_E + K_P}$$

$$a_W = \frac{k_w}{\Delta X}\Delta Y \qquad k_w = \frac{2K_W K_P}{K_W + K_P}$$

$$a_N = L^2\frac{k_n}{\Delta Y}\Delta X \qquad k_n = \frac{2K_N K_P}{K_N + K_P} \tag{61}$$

$$a_S = L^2\frac{k_s}{\Delta Y}\Delta X \qquad k_s = \frac{2K_S K_P}{K_S + K_P}$$

$$a_P = a_E + a_W + a_N + a_S$$

$$S_c = U(C_w - C_e)\Delta Y$$

The values of *k* at the surface boundaries of the control volume are evaluated by utilizing the harmonic mean, as suggested by Patankar (1980), as a means of maintaining continuity.

The discretization for the critical shear stress, Case III, is done in the same manner as for the Navier slip, Case I. The only difference between the coefficients of Case I and Case III, occurs in the term S_c. For the Case III, S_c includes shear stress terms as shown in Equation (62).

$$S_c = U(C_w - C_e)\Delta Y - T(B_w - B_E) \pm T(B_S - B_N) \tag{62}$$

Where the coefficient B is substituted for the quantity:

$$\left(\frac{AH^2}{H + A}\right) = B \tag{63}$$

Journal Bearing

The same method is used to discretize the governing equation for the journal bearing with two major differences. First, instead of pressure, the unknown variable being solved for is ϕ. Second, the upwind scheme is used to minimize instabilities created by discontinuities at the boundaries of the cavitation region (Patankar 1980). The discretized equation is,

$$a_P\phi_P = a_E\phi_E + a_W\phi_W + a_N\phi_N + a_S\phi_S + S_C \tag{64}$$

The corresponding coefficients for the journal bearing discretization are summarized in Equation (65).

$$
\begin{aligned}
a_E &= k_e(F_e)\frac{\Delta Y}{\Delta\theta} \qquad k_e = \frac{2K_E K_P}{K_E + K_P} \\
a_W &= k_w(F_w)\frac{\Delta Y}{\Delta\theta} \qquad k_w = \frac{2K_W K_P}{K_W + K_P} \\
a_N &= k_n(F_n)\frac{\Delta\theta}{\Delta Y} \qquad k_n = \frac{2K_N K_P}{K_N + K_P} \\
a_S &= k_s(F_s)\frac{\Delta\theta}{\Delta Y} \qquad k_s = \frac{2K_S K_P}{K_S + K_P} \\
a_P &= a_E + a_W + a_N + a_S + S_P \\
S_P &= \gamma(C_e)(1 - F_P)\frac{\Delta Y}{2} \\
S_C &= \gamma(C_e)\frac{\Delta Y}{2}
\end{aligned}
\tag{65}
$$

Solution Method

Having broken the problem into a discrete set of equations the next step is to solve those equations iteratively. The Alternating-Direction Implicit method (ADI) is used to do this. In this method one line of nodes is examined at time, while nodes on neighboring lines are assumed to be known values and remain constant. The solution proceeds along all lines in one direction then switches to lines in the perpendicular direction.

Using the ADI iterative method, the problem along a single line can be solved with a Tri-Diagonal Matrix Algorithm (TDMA). This algorithm is described in detail by Patankar (1980).

Slider Bearing

A schematic for the overall program for the plane pad bearing under the Navier slip condition is included in Figure 7. As with the two other cases the program starts off with a declaration of operating parameters and mesh specification. The Reynolds equation coefficients are then computed and the unknown variable, here the pressure, is initialized. The solution then enters the ADI scheme using a loop for the iterative method until the result meets the convergence criteria. For this project a convergence criteria was set at a percent difference between iterations of $1x\ 10^{-6}$. Once convergence is determined the data is output and the performance parameters are calculated.

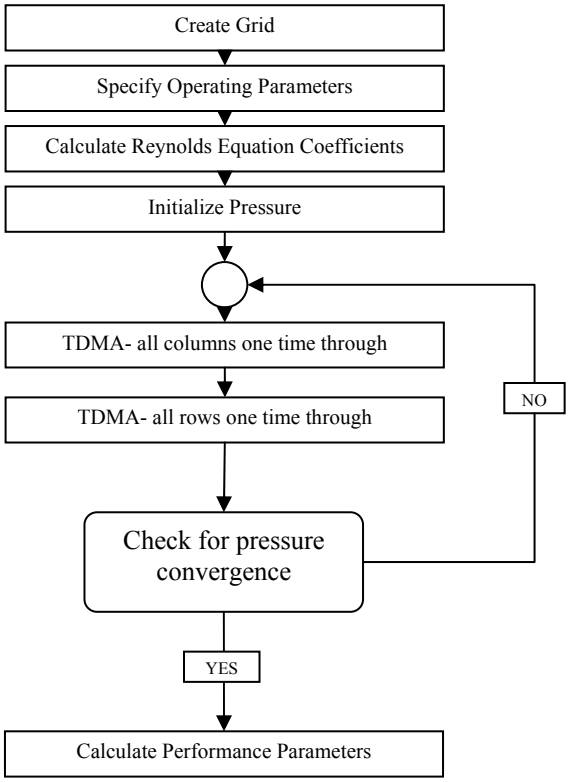

Figure 7- Flow chart for program of slider bearing under Navier slip condition

For Case III an additional loop is added to iteratively check the boundary shear stress for the slip condition. A schematic for this program is below in Figure 8.

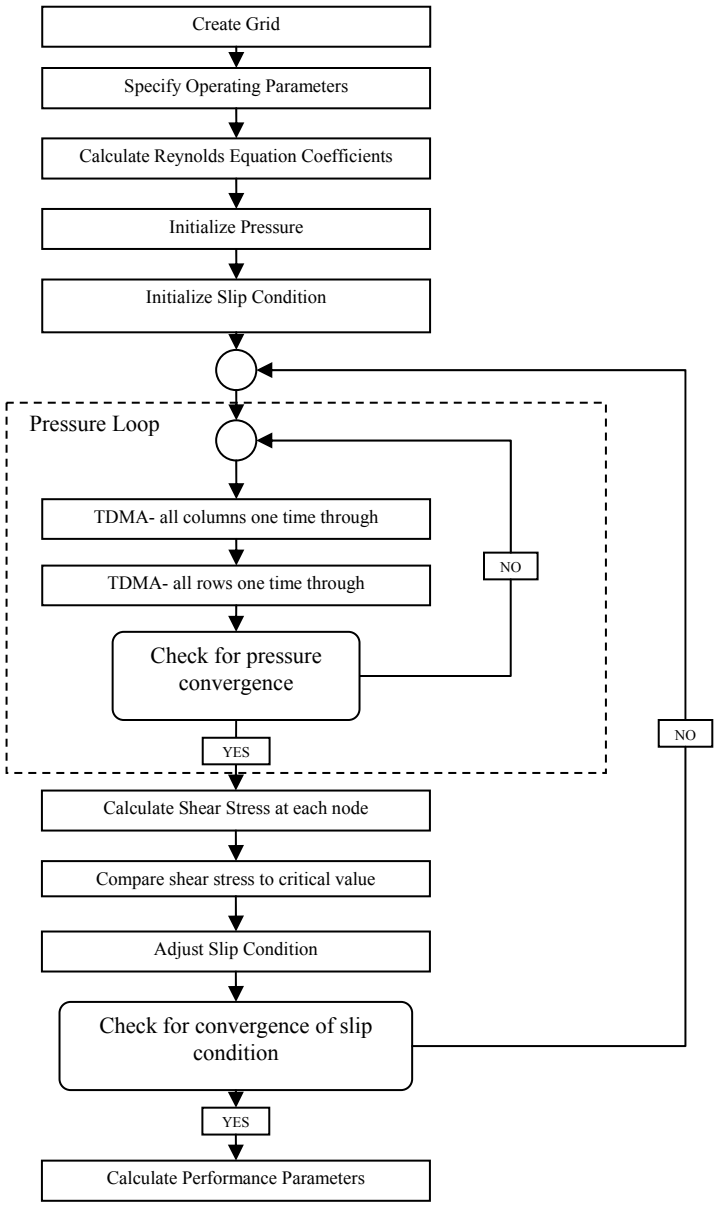

Figure 8- Flow chart for program of slider bearing with critical shear stress condition

Journal Bearing

In the Case II the program is solved for *F* and ϕ instead of pressure. A flow chart is shown in Figure 9.

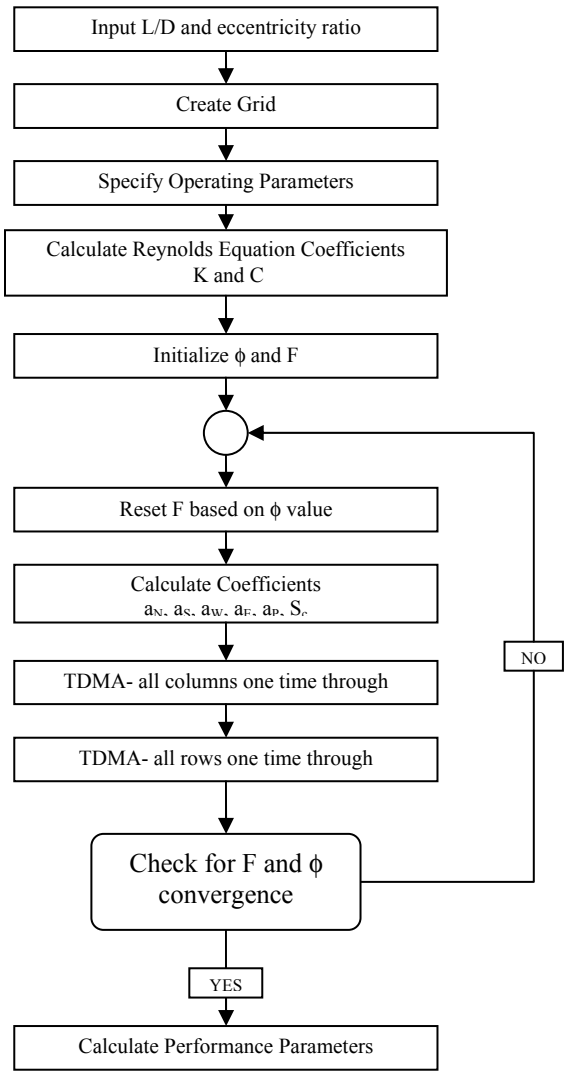

Figure 9- Flow chart for program of journal bearing with Navier slip condition

CHAPTER 4

RESULTS

4.1 Case I – Slider Bearing with Navier Slip Condition (Salant and Fortier 2004)

Developing a representative bearing

In order to facilitate comparison, a representative bearing is developed that establishes base values for geometry and operating parameters.

For the plane pad bearings the representative bearing has the following attributes:

1.) The overall dimensions of the bearings are chosen such that the ratio of bearing length to width is 1.0.
2.) The incline of Surface 2 is set so that the ratio of inlet film thickness to outlet film thickness is 1.25.
3.) The driving velocity of Surface 1 is set at the dimensionless U value of 50.

For the instances when a pattern is applied to Surface 2, base values are assigned to the dimensions of Regions I. Region I remains situated as previously described. The base length for Region I is 0.725 times the total bearing length. The base width is set to 0.75 of the total width of the bearing.

In analyzing the effect of slip a number of bearing types will be considered. One of these is a bearing with a recess in Region I. For those bearings the base value set for dimensionless recess depth is 0.19. For bearings where slip occurs in Region I, the base value for the dimensionless slip coefficient is 100.

These representative bearing attributes are shown graphically below in Figure 10.

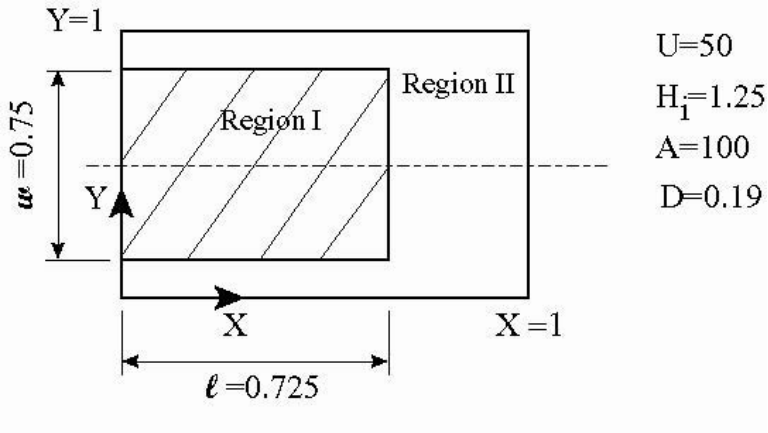

Figure 10- Diagram of representative plane pad bearing attributes

When not explicitly stated the bearings considered in this analysis can be assumed to possess the base attributes.

Comparison of Pressure Profiles

Consider a plane pad bearing conforming to the base attributes with slip applied in Region I. The load carrying capacity computed for this bearing is W=1.291. For a

conventional bearing of the same configuration but without any slip (A=0) the corresponding load support is W=0.312. In this instance, the load support gained by the addition of slip is three times that of the conventional bearing alone.

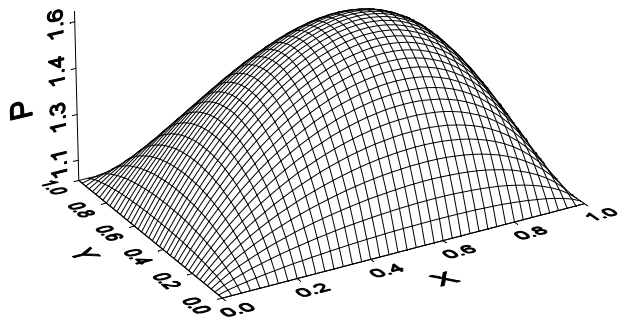

Figure 11- Pressure profile for Case I conventional bearing, L=1, H_i=1.25, U=50

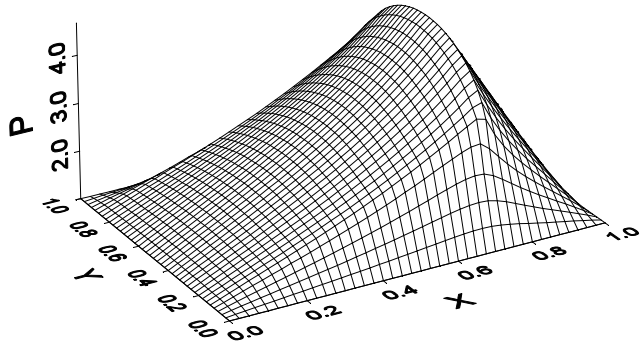

Figure 12-Pressure profile for Case I bearing with slip in Region I, A=100, L=1, Hi=1.25, U=50

The pressure profile for the bearing with slip is shown in Figure 12 while Figure 11 shows that of the conventional bearing. There is a distinct difference in the shape of two

pressure profiles corresponding to the area in which the slip pad is situated. Additionally the bearing with slip reaches a maximum pressure which is over twice that achieved by the conventional bearing alone.

The pressure distribution for a bearing with a recess in Region I is shown in Figure 13. Note that the pressure distribution is very similar to that found for the bearing with slip. This similarity follows from the mechanism at work in these bearings. Both the recess and the slip surface act to reduce the resistance to flow in the region to which they are applied. In both cases, the fluid flows from a region of low flow resistance to a region of high flow resistance. It is the sudden increase in flow resistance at the boundaries of the two regions that produces the load support. The load support for the bearing with recess is W=0.523 while the load support with the slip pad is W=1.291. The bearing with slip, therefore, shows a significant advantage over the bearing with recess for this base configuration.

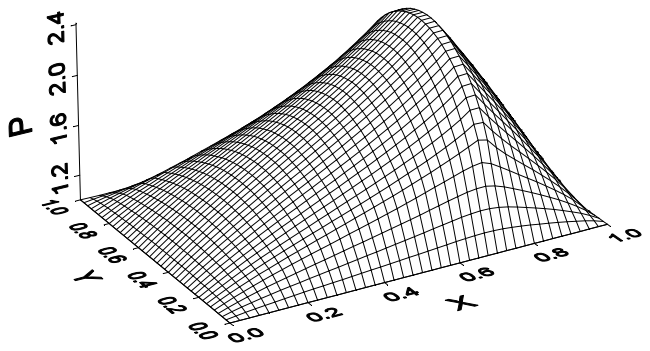

Figure 13- Pressure profile for Case I bearing with recess in Region I, D=0.19, L=1, H_i=1.25, U=50

Parametric Study

A parametric study is performed to characterize bearing performance with respect to a number of operating parameters. For this analysis four bearings are considered; one with slip applied in Region I, one with a recess applied in Region I, a conventional no-slip bearing and one with both slip and a recess applied to Region I. The bearings follow the base attributes of the previous section, with one attribute of interest being varied at time.

For the plane pad bearing the effect of changing driving velocity, slip coefficient, slope of incline and recess depth are evaluated with regard to bearing load carrying capacity, side leakage rate and friction force.

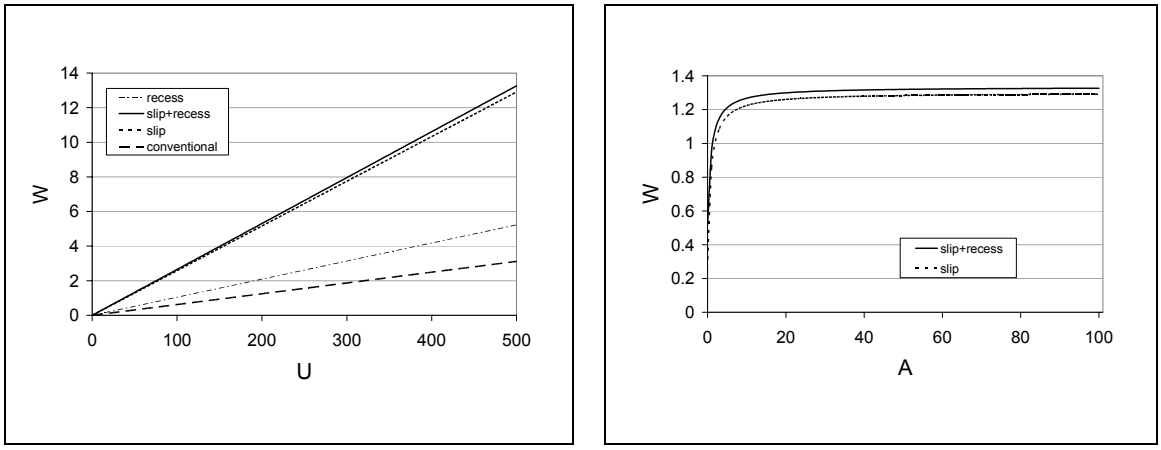

(a.) (b.)

Figure 14- Results of parametric analysis on load in plane pad bearings; (a.) load vs. speed (b.) load vs. slip coefficient

Figure 14 (a.) shows the effect of changing the dimensionless speed, U, on load carrying capacity, W. Load is found to have a linear variation with speed. When no driving speed is present (U=0), there is zero load support for all four bearing configurations. By

the time U reaches a value of 5 the bearings with slip show a significantly higher load than those without slip. The load supported by the bearing with both a recess and slip consistently achieves a load carrying capacity that is 2.5 times that of the bearing with the recess alone.

Figure 14 (b.) shows the variation of load carrying capacity as a function of the dimensionless slip coefficient, A. It's found that after A reaches a value of 10, subsequent increases in the slip coefficient have little effect on the resulting load. This suggests that as long as a slip surface can achieve a slip coefficient in this range the maximum benefit, with regard to load carrying capacity, is gained.

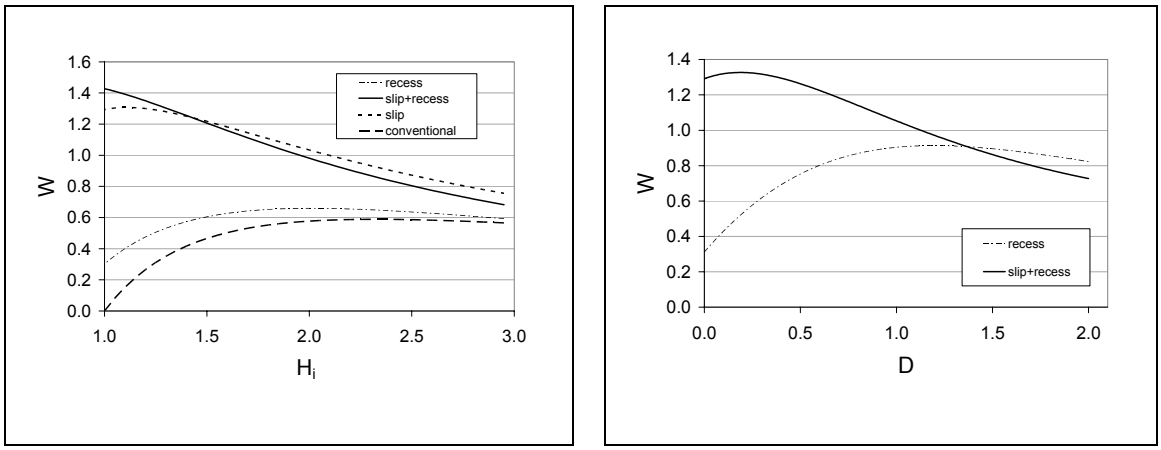

(a.) (b.)

Figure 15- Results of parametric analysis on load in plane pad bearings; (a.) load vs. incline (b.) load vs. recess depth

Figure 15 (a.) is a graph of the variation of load carrying capacity with respect to the dimensionless parameter H_i. H_i is the ratio of inlet to outlet film thickness and therefore starts at a value of 1, which represents parallel surfaces. Each bearing configuration exhibits slightly different behavior with changing H_i. The conventional bearing has zero

load carrying capacity when the surfaces are parallel. Load then increases with increasing slope until its maximum value is attained at H_i=2.3, then it begins to decrease. The bearing with recess alone shows a similar trend. For this bearing the load carrying capacity starts out at a value of 0.3 increases to a maximum at H_i= 2 and decreases thereafter. The bearing with slip alone starts off with a high load carrying capacity with parallel surfaces of W=1.3, A slight increase occurs until the maximum value is reached at H_i=1.1. The load falls off steadily as H_i continues to increase. For the bearing with slip and recess the maximum load carrying capacity occurs at H_i of 1 and decreases as H_i is increased.

Figure 15 (b.) shows the variation of load carrying capacity with respect to dimensionless recess depth for bearings with and without slip. Both curves are found to have optimal values of D which result in the max load carrying capacity. For the bearing without slip the maximum occurs at D=1.19, which is on the order of what would be expected as optimal for a Rayleigh step bearing. The addition of slip to the bearing causes not only the magnitude of the maximum load to be higher but for it to occur at a much smaller value of D=0.19, after which the load falls off steadily. Another surprising attribute of this graph is the crossing of the curves. It would be expected that as the depth of the recess increased the effect due to slip would diminish because the shear stress driving the slip would decrease. Why then doesn't the curve asymptotically approach the curve corresponding to the recess alone? There must be some mechanism by which the slip at high depth is becoming a liability in terms of load carrying capacity.

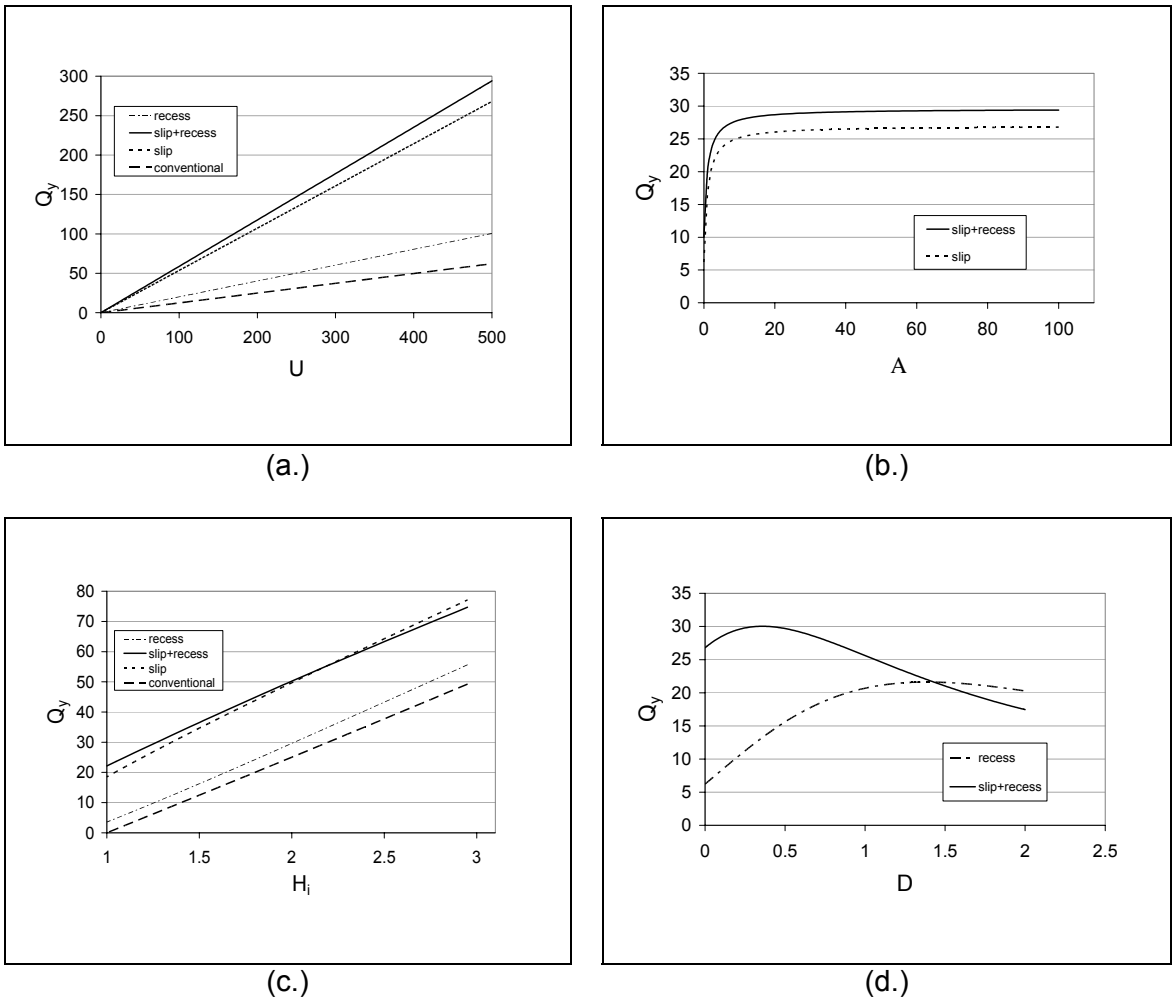

Figure 16- Results of parametric analysis on side leakage in plane pad bearings; (a.) side leakage rate vs. speed (b.) side leakage rate vs. slip coefficient (c.) side leakage rate vs. incline (d.) side leakage rate vs. recess depth

Figure 16 (a.)-(d.) show the side leakage, Q_y, as a function of the previously discussed parameters. The side leakage behaves in a manner consistent with load carrying capacity for changing speed, slip coefficient, and recess depth. In the case of changing H_i, the side leakage increases linearly with H_i in all four bearing configurations.

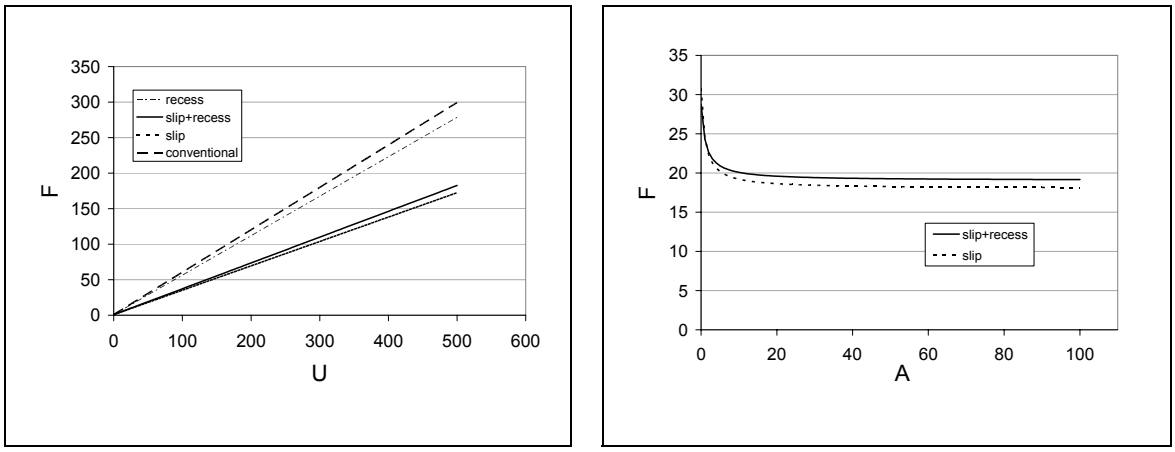

(a.) (b.)

Figure 17- Results of parametric analysis on friction force in plane pad bearings (a.) friction force vs. speed (b.) friction force vs. slip coefficient

The results for friction force are shown in Figure 17 and Figure 18. As in the case of load carrying capacity and side leakage, the friction force increases linearly with speed. Friction is found to be lower for the bearings with slip than those without. Above a speed of U=100, the bearing with the recess alone generates a friction force 1.5 times larger than the force generated by the bearing with the recess slip combination. Figure 17 once again exhibits the asymptotic nature of variation with respect to slip coefficient. In the case of the friction force however the value starts off high for no-slip and then decreases toward the final value.

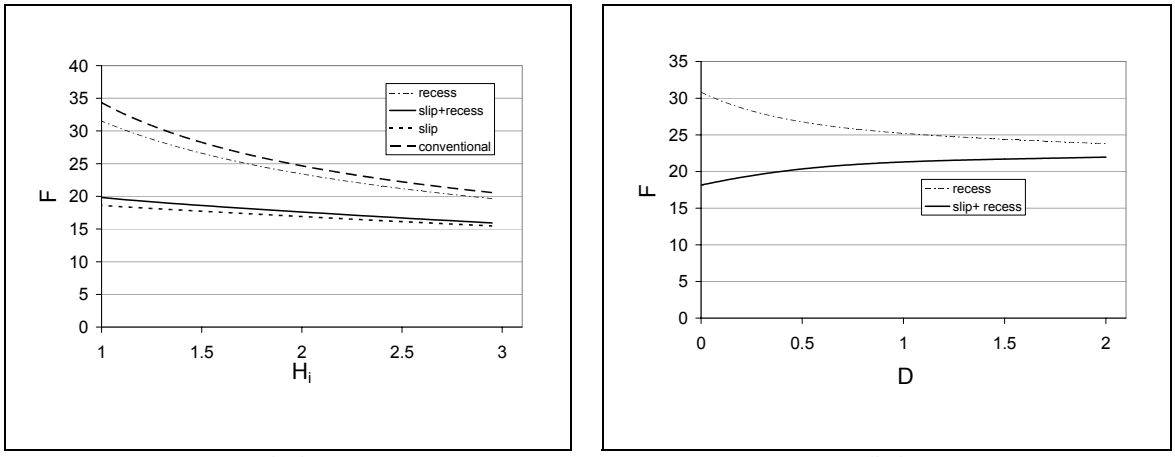

(a.) (b.)

Figure 18- Results of parametric analysis on friction force in plane pad bearings (a.) friction force vs. incline (b.) friction force vs. recess depth

Figure 18 (a.) shows the relationship between friction force and H_i. In all four bearing configurations the friction forces decreases as the incline becomes steeper. In Figure 18 (b.) the results for friction force with respect to recess depth are shown. The two curves appear to approach each other as recess depth increases; the bearing with slip increasing in friction, the bearing without slip decreasing.

Optimized Configuration

Up to this point the analysis for Case I has been done using a single representative bearing configuration. In an effort to expand the comparison between the four plane pad bearings of the parametric study, the optimal bearing geometry is found for each in terms of load carrying capacity. The bearing characteristics for the optimal geometries are presented in Table 1.

Table 1- Optimal performance for four plane pad bearings, U=50, A=100

bearing type	W	Q_y	F	H_i	ℓ	ω	D
conventional	0.589	32.6	23.1	2.3	———	———	———
recess	0.988	16.8	25.2	1.0	0.750	0.75	1.50
slip	1.327	18.6	20.4	1.0	0.625	0.75	———
slip + recess	1.451	23.3	20.6	1.0	0.725	0.75	0.33

The geometric parameters that are reevaluated for optimization are the incline of Surface 2, the length and width of Region I and the recess depth. The results for optimal incline of the conventional bearing are consistent with theory (Williams 1994). The bearing with recess has an optimal incline parameter of 1 which corresponds to a parallel surface configuration. It also has an optimal recess depth of 1.5. This recess depth is on the order of that expected for a Reyleigh step bearing, 0.866 (Hamrock 1994). The real areas of interest, however, are in the optimal configuration of the bearings with slip. Both the bearing with slip alone and the slip and recess combination have achieve their maximum load carrying capacity with parallel surfaces.

These results for load carrying capacity enforce earlier findings. The bearings with slip in their optimal geometric configuration provide significantly more load support that those without.

The results for friction force varied little between the four bearing types. All the values fell between 20 and 26. The bearings with slip generated lower friction forces than those without slip.

4.2 Case II- Journal Bearing with Navier Slip Condition

Developing a representative bearing

For the journal bearing a new set of base values describing a representative bearing are chosen. In this case the over all dimensions are set relative to each other so that the length to diameter ratio is 1. The eccentricity ratio, ε is set to a base value of 0.6, keeping it in the mid range. The dimensionless quantity for speed, γ, is set at 5, and the slip coefficient A is set to 100 in cases where slip occurs. These base values are summarized below in Figure 19.

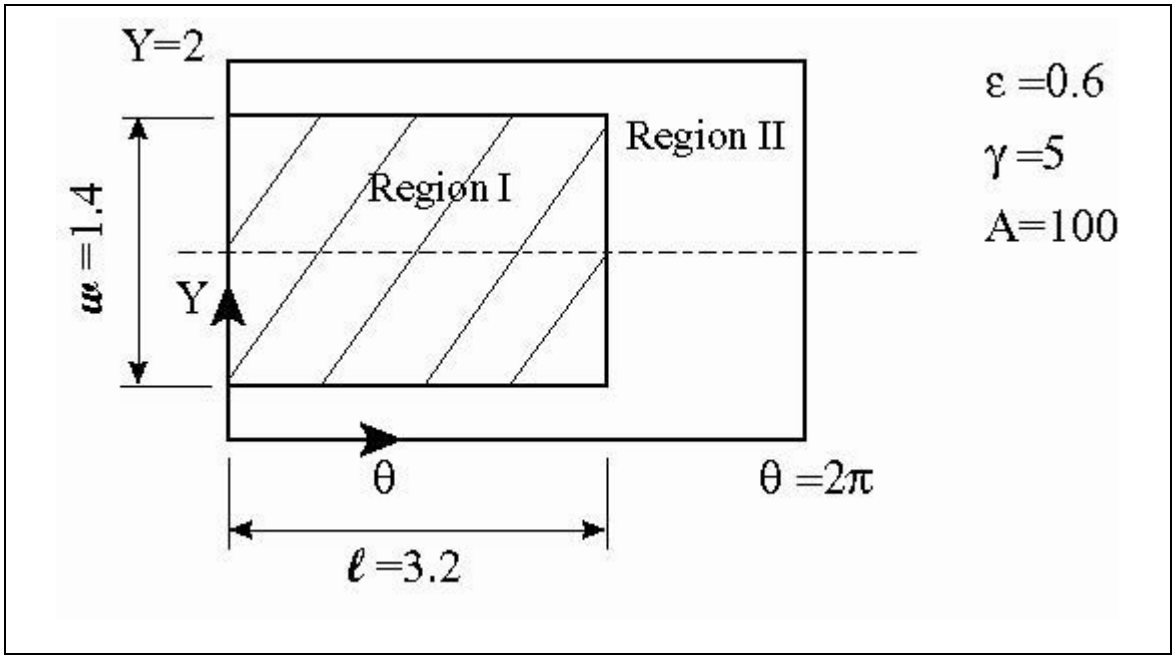

Figure 19- Representative bearing attributes used for the analysis of Case II

An analysis is done to find the best dimensions for the slip pad. There are two ways used to define “best”. The first way is to minimize the Sommerfeld number. These pad dimensions maximize the load carrying capacity of the bearing. The dimensions corresponding to this optimization method are ℓ = 3.2, ω = 1.4, where l is the length of the slip pad in radians and w is the width of the slip pad non-dimensionalized by the bearing radius.

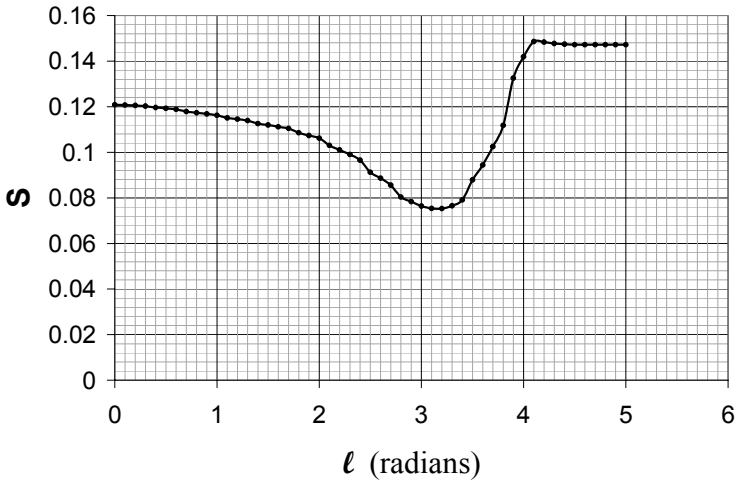

Figure 20- Graph of Sommerfeld number as a function of slip pad length for application in a representative journal bearing, ω=1.4

Figure 20 shows the effect of slip pad length on Sommerfeld number. The Sommerfeld number starts at ℓ = 0 with the no-slip value of 0.121. From there it decreases until ℓ = 3.2, just after the point of minimum film thickness has been reached. As the slip pad extends into the cavitation regime the Sommerfeld number increases again until it reaches a plateau at ℓ = 4.1.

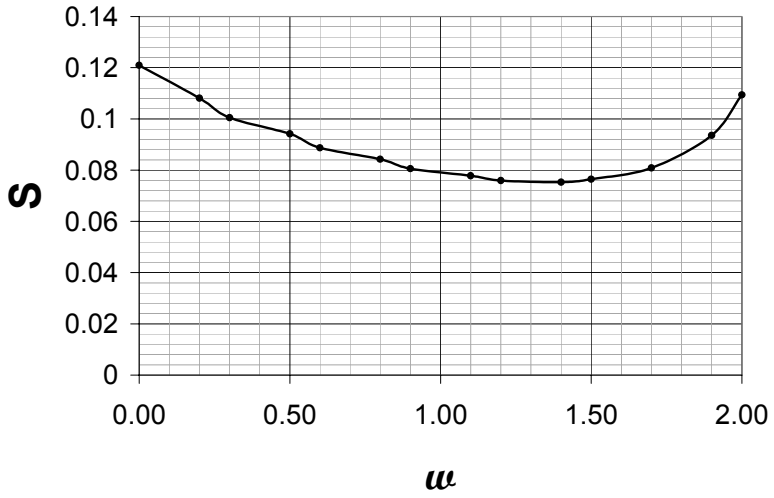

Figure 21- Graph of Sommerfeld number as a function of slip pad width for application in a representative journal bearing, ℓ=3.2

The effect of slip pad width on Sommerfeld number is shown in Figure 21. This graph shows the advantage gained by having the no-slip margins along the sides of the bearing. The Sommerfeld number corresponding to the completely no-slip case is 0.121. The Sommerfeld number corresponding to slip applied to the full width is 0.109. The two values are very close to one another with the slip adding only a small advantage in terms of load. The Sommerfeld number for the optimal width (ω = 1.4) is S=0.075, a significant advantage over the other two options.

The second method is to minimize the friction coefficient. The smallest friction forces and friction coefficient occurs when the slip pad covers the entire area of Surface 1. From the perspective of load support however, this configuration is not practical. The Sommerfeld number for the bearing allowing slip on the full surface is very large, S=0.242, implying a small load capacity. In order to minimize the frictional losses of the bearing it is therefore advantageous to make the slip pad as large as possible while balancing the effect on load support.

In the subsequent analysis of the journal bearing the base dimensions used for the slip pad area are those corresponding to minimum Sommerfeld number, ℓ = 3.2, ω = 1.4.

Comparison of Pressure Profiles

Consider a journal bearing conforming to the base attributes with slip applied in Region I. The Sommerfeld number computed for this bearing is S=0.075. For a conventional journal bearing of the same configuration but without any slip (A=0) the corresponding Sommerfeld number is S=0.121. In this instance, the load support gained by the addition of slip is 1.6 times that of the conventional bearing alone. As in the case of the plane pad bearing, the pressure profiles differ in the region where slip is applied.

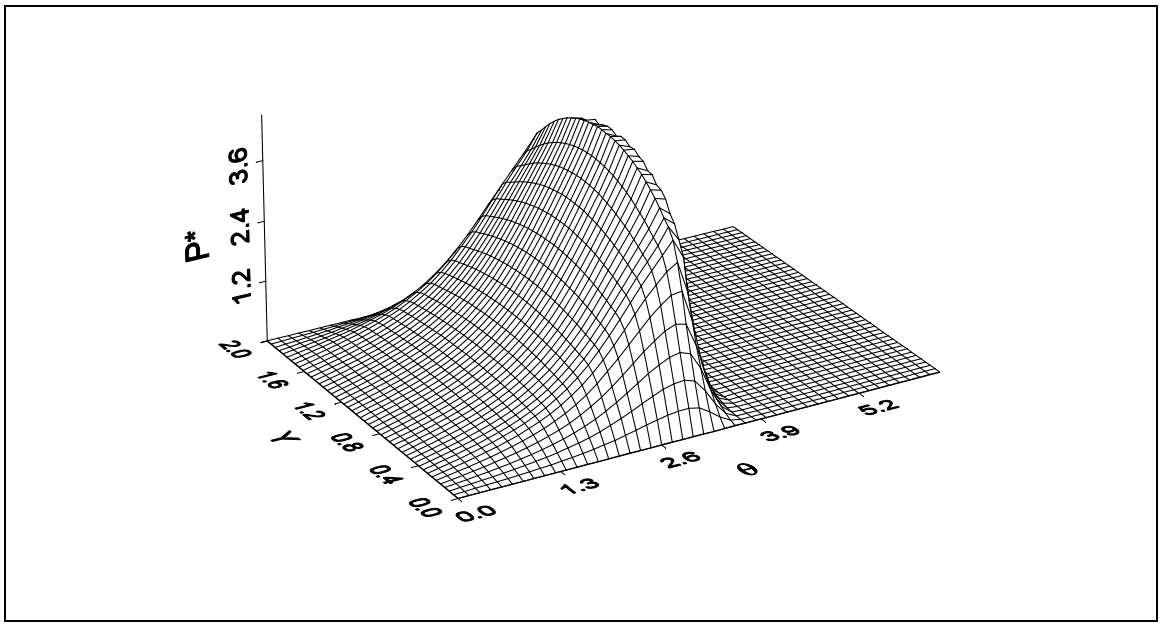

Figure 22- Pressure profile for Case II with Slip applied, S=0.075

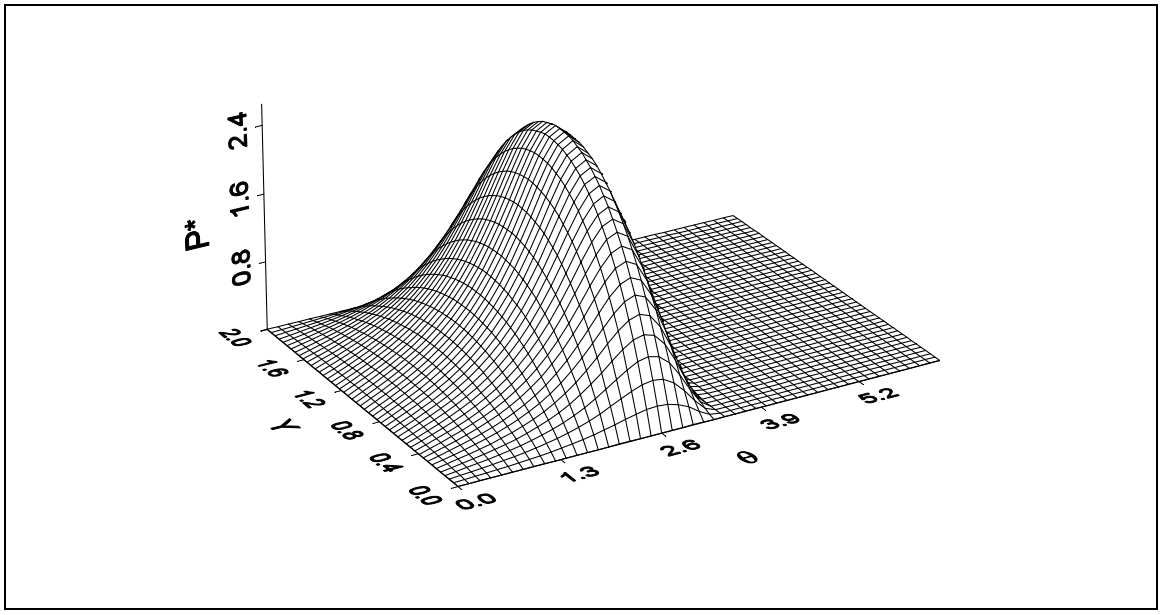

Figure 23- Pressure Profile for Case II with no slip, conventional journal bearing, S=0.121

Parametric Study

Two parameters are analyzed for their effect on journal bearing performance. The first is the slip coefficient, here evaluated in its dimensionless form, A. The second is the driving speed of the bearing represented by the dimensionless parameter, γ.

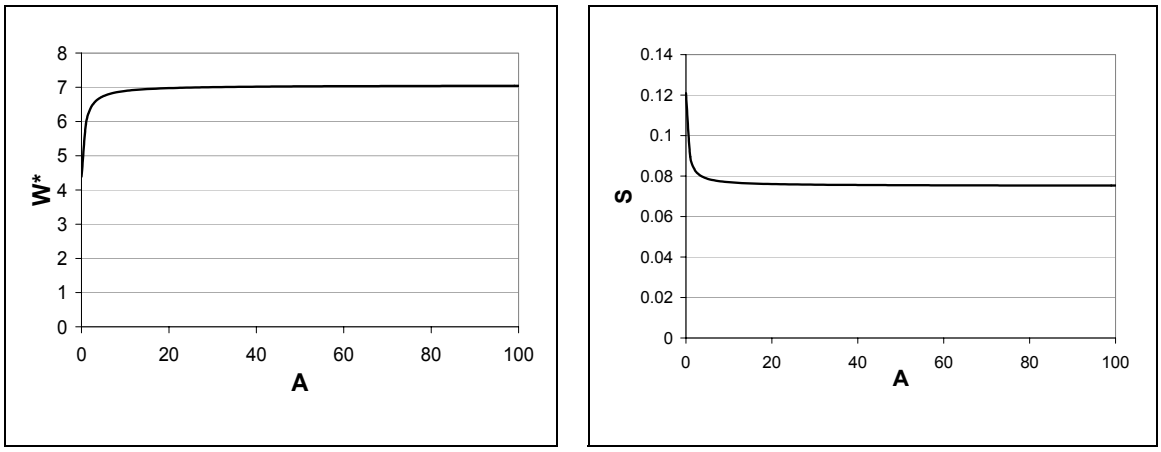

(a.) (b.)

Figure 24- Effect of changing the slip coefficient on journal bearing performance parameters (a.) load (b.) Sommerfeld number

Figure 24 (a.) and (b.) are graphs of the data for dimensionless load and Sommerfeld number as a functions of slip coefficient, A. As was seen in Case I, the slip coefficient has an insignificant effect on load capacity after a value of 10 is exceeded.

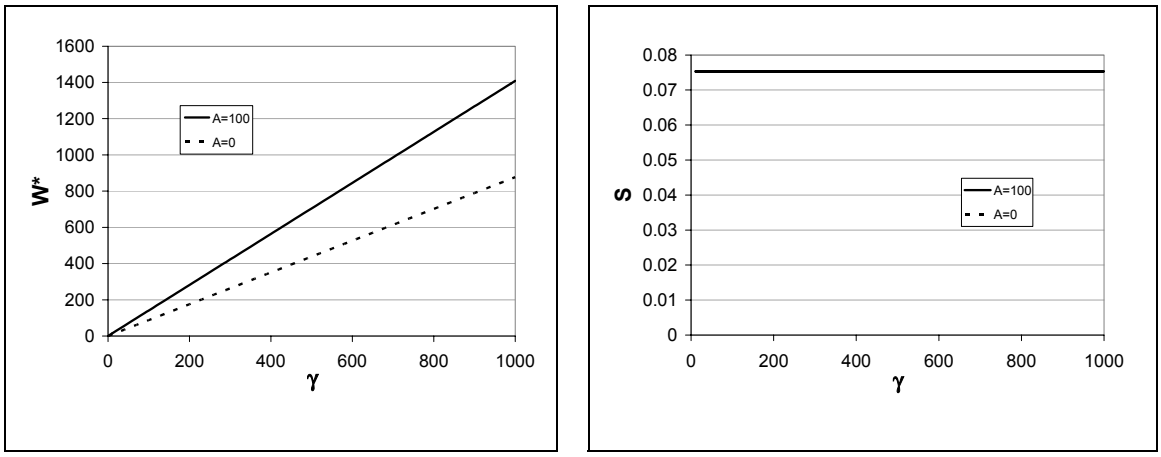

(a.) (b.)

Figure 25- Effect of changing the speed on journal bearing performance parameters (a.) load (b.) Sommerfeld number

In Figure 25 the effect of changing γ is shown. Since γ is a dimensionless quantity representing the driving speed, the linear relationship found with dimensionless load is similar to the results for Case I. For this base configuration, the load carried by a bearing with slip is consistently 1.6 times that carried by a bearing without slip at the same speed. The Sommerfeld number is constant with respect to speed. This is expected because the Sommerfeld number is directly proportional to the ratio of γ to W*, and W* is proportional to γ.

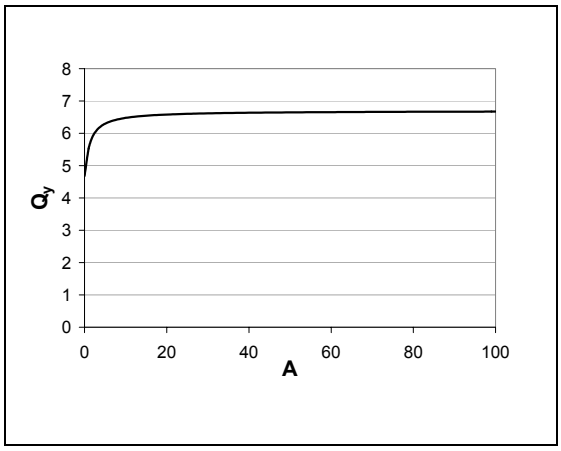

(a.)

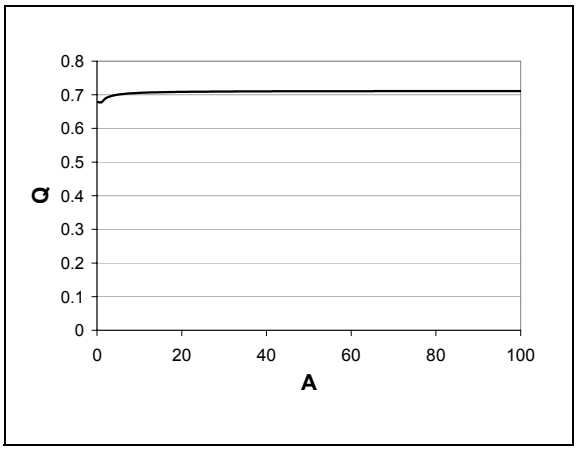

(b.)

Figure 26- Effect of changing the slip coefficient on journal bearing performance parameters (a.) Q_y (b.) Q

The results for side leakage are consistent with the expectations based on the results for the load. Figure 25 and Figure 26 give a graphical representation of these results. Once again the same asymptotic behavior is seen with respect to slip coefficient, A, and a linear behavior is found for dimensionless side leakage rate, Q_y, with respect to γ. Q is independent of gamma and is equal to 0.71 with slip, 0.68 without slip.

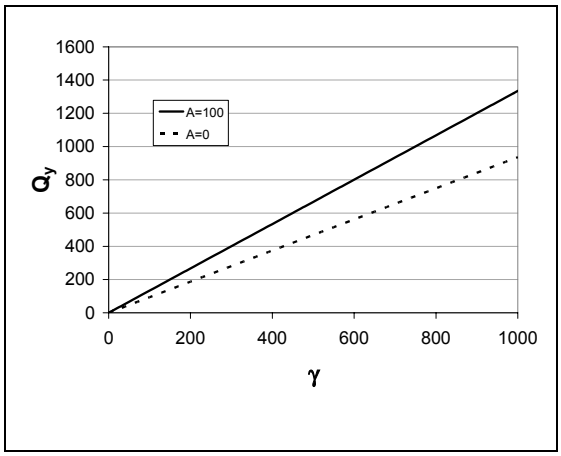

(a.)

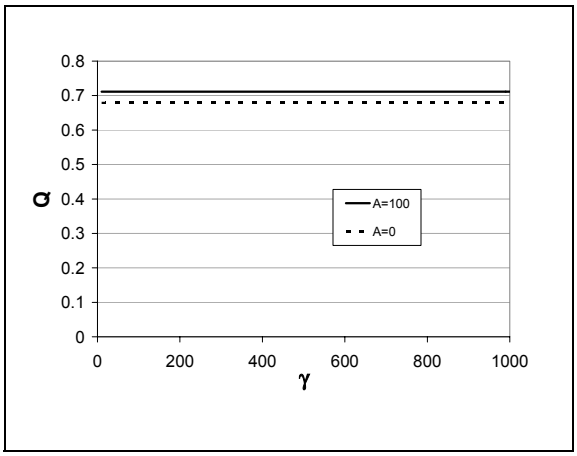

(b.)

Figure 27- Effect of changing the speed on journal bearing performance parameters (a.) Q_y (b.) Q

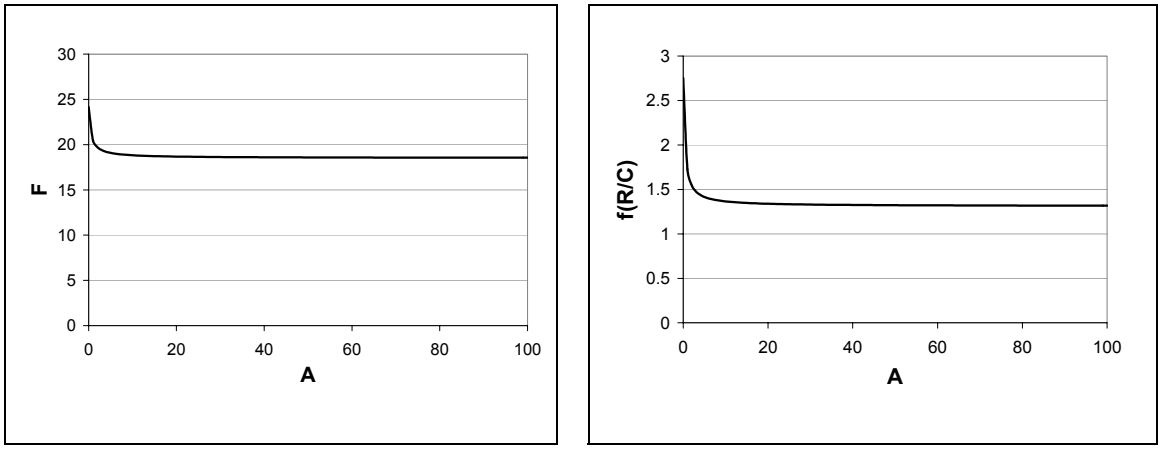

(a.) (b.)

Figure 28- Effect of changing the slip coefficient on journal bearing performance parameters (a.) friction force (b.) friction coefficient

The results for friction are similar to those for Case I. Figure 28 shows the variation of the dimensionless friction force and friction coefficient with respect to slip coefficient. In both cases the friction is greatest in the no-slip case (A=0), and decreases to a constant value by A=10.

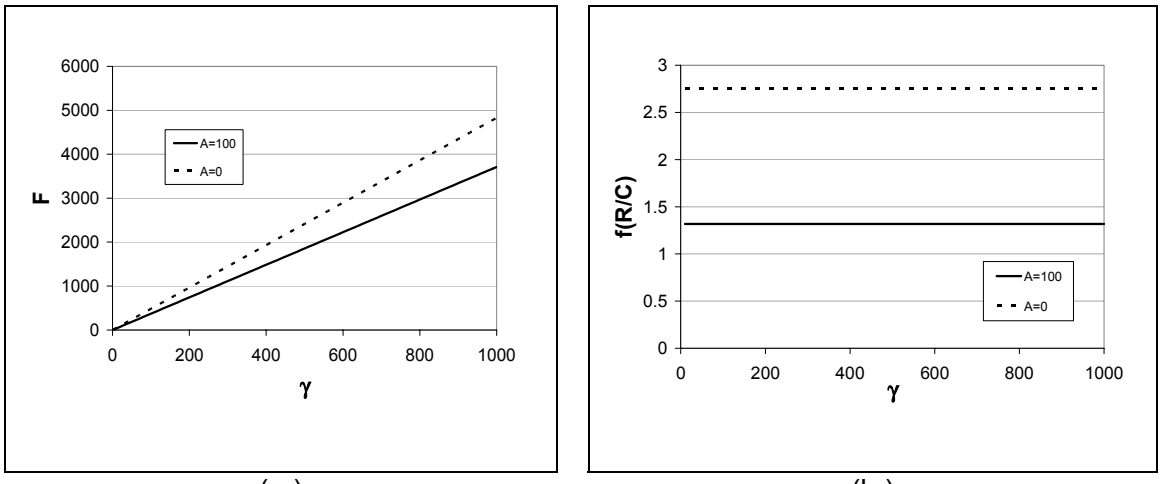

(a.) (b.)

Figure 29- Effect of changing the speed on journal bearing performance parameters (a.) friction force (b.) friction coefficient

The friction force exhibits a linear variation with γ as seen in Figure 29. The friction factor parameter *f(R/C)* has a constant value, independent of γ, of 2.7 and 1.3 for the no-slip and slip bearings respectively.

Standard Graphs

The standard graphs used to represent performance parameters were developed by Raimondi and Boyd (1958). Similar graphs for the conventional no-slip journal bearing are presented here along side the graphs for bearings with slip imposed.

Figure 30, Figure 31, and Figure 32 show the graphs for eccentricity ratio, friction coefficient and leakage rate respectively. Each is graphed as function of Sommerfeld number. The four curves in each graph correspond to a different bearing length to diameter ratios.

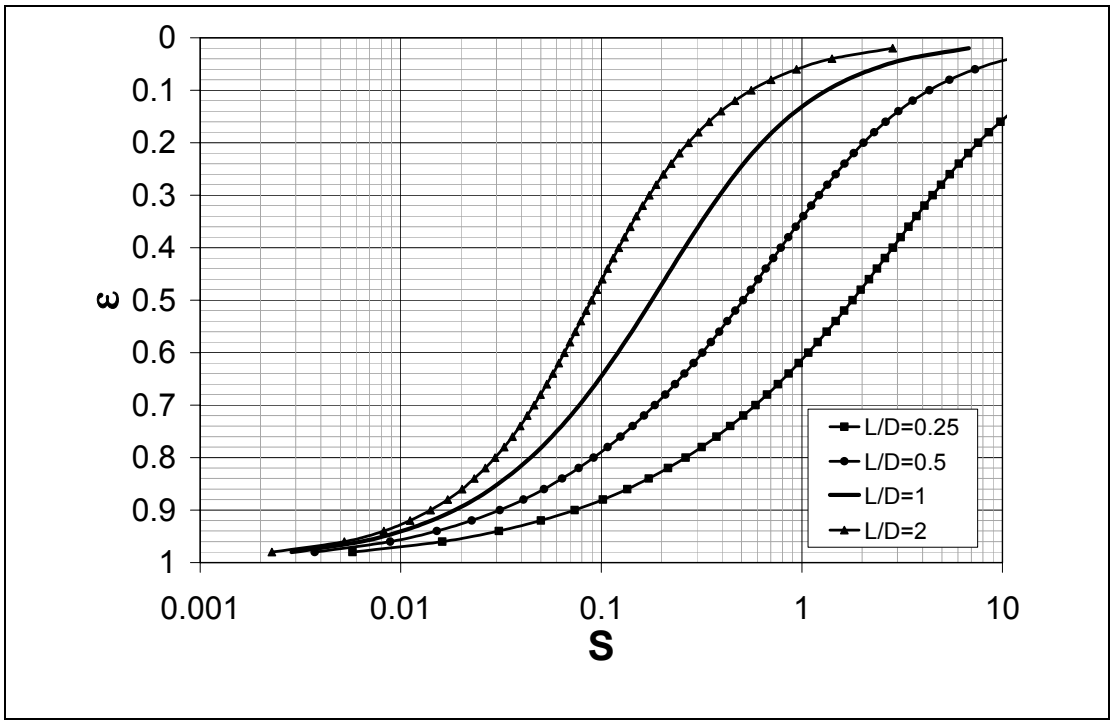

(a.)

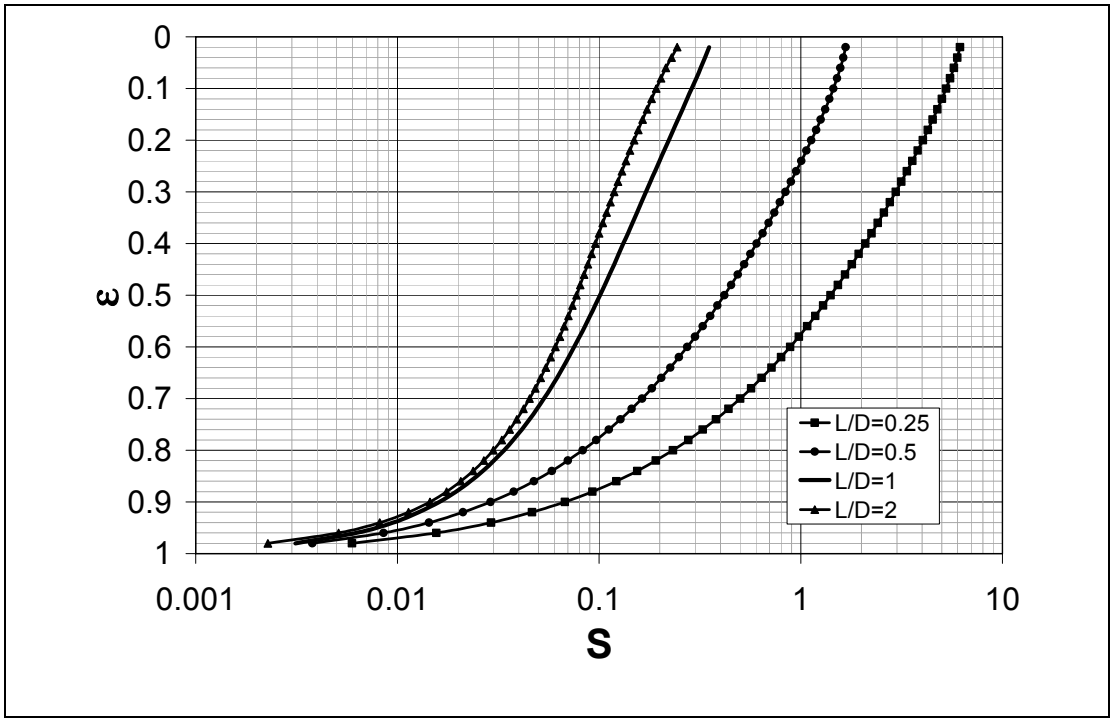

(b.)

Figure 30- Comparison of Raimondi and Boyd graphs for eccentricity ratio vs. Sommerfeld number (a.) bearings without slip (b.) bearings with slip

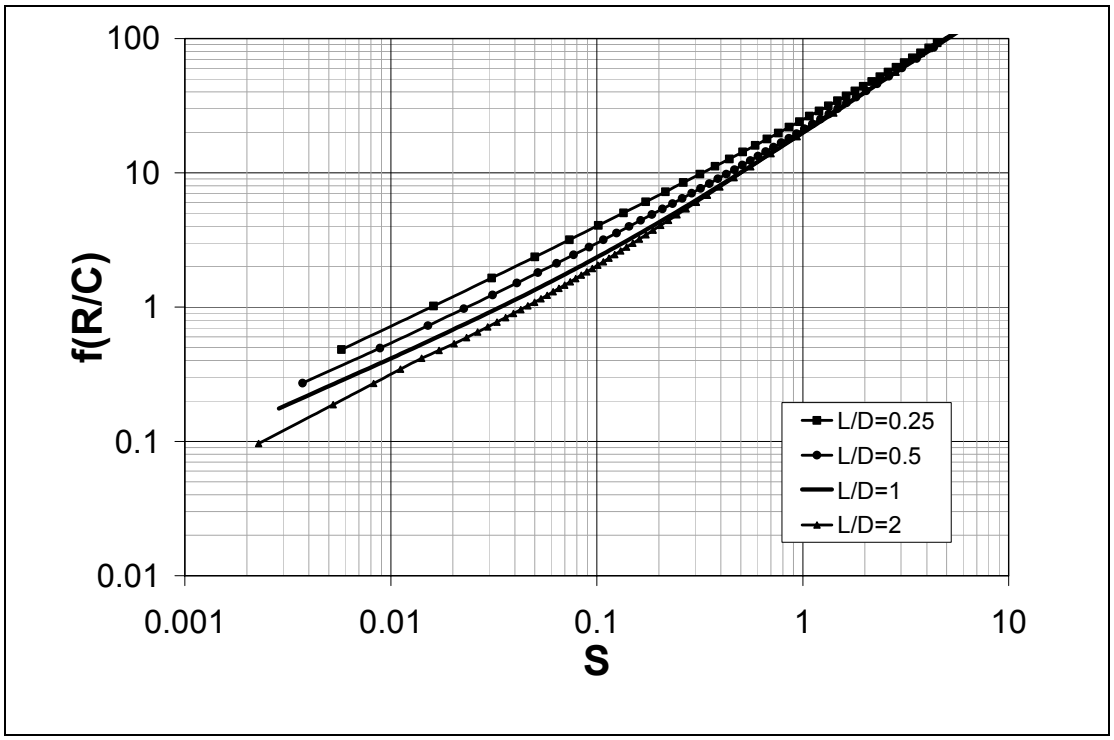

(a.)

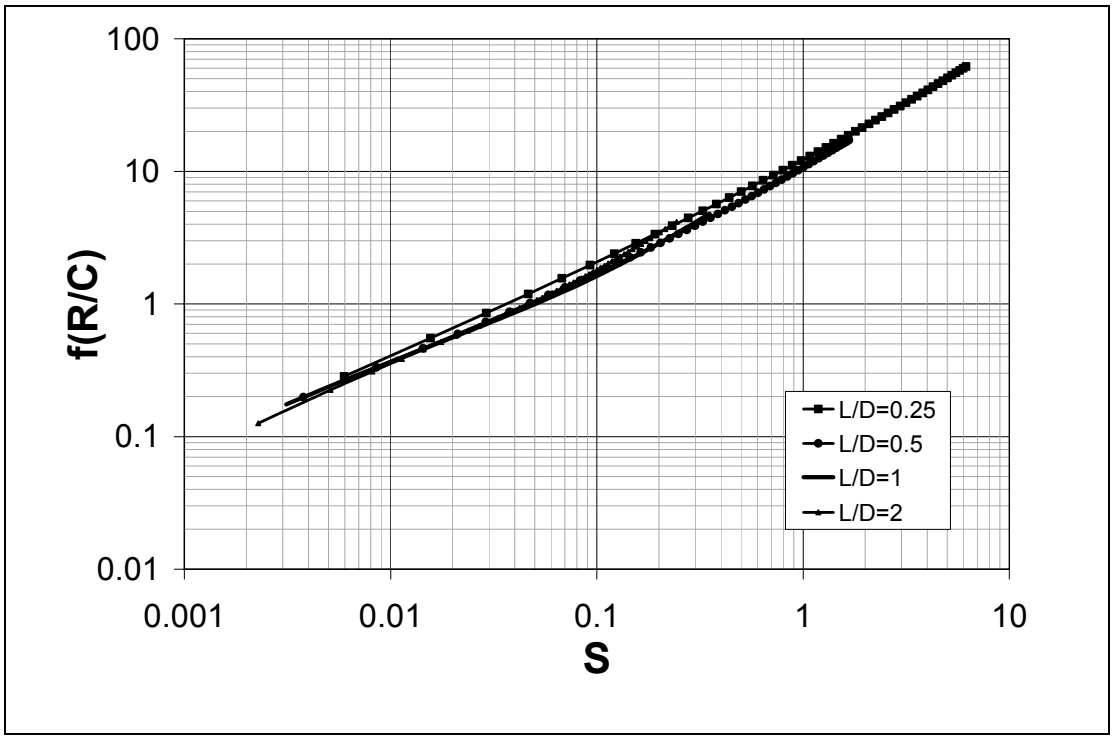

(b.)

Figure 31- Comparison of Raimondi and Boyd graphs for friction coefficient vs. Sommerfeld number (a.) bearings without slip (b.) bearings with slip

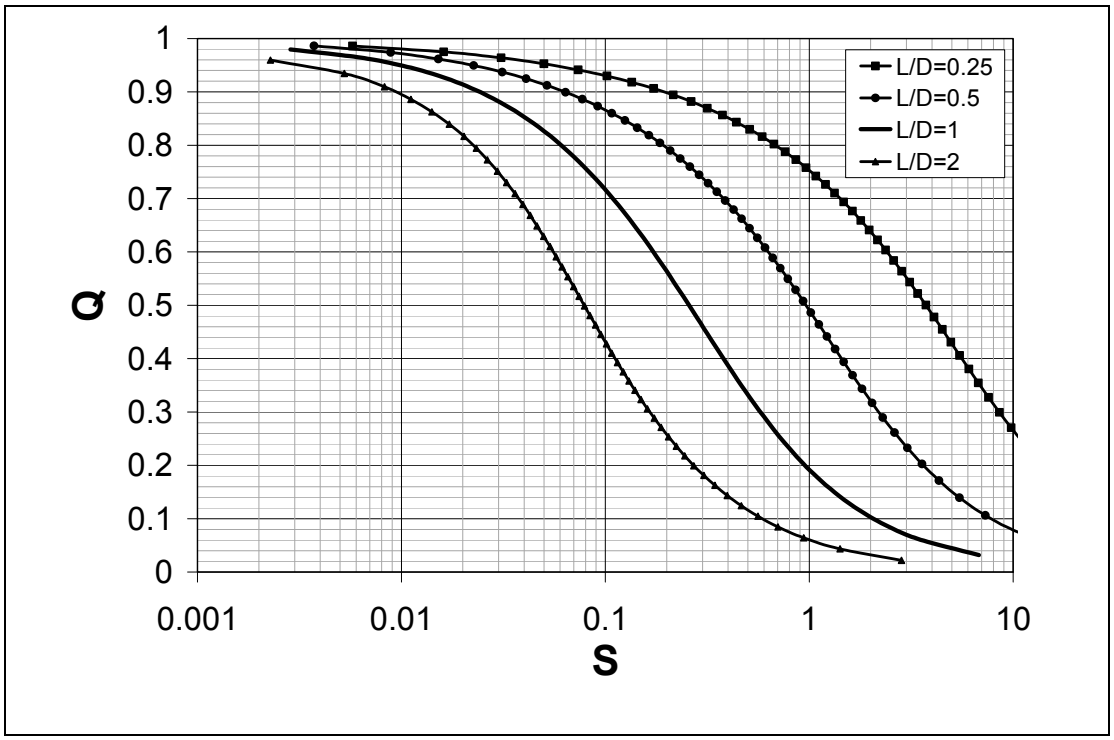

(a.)

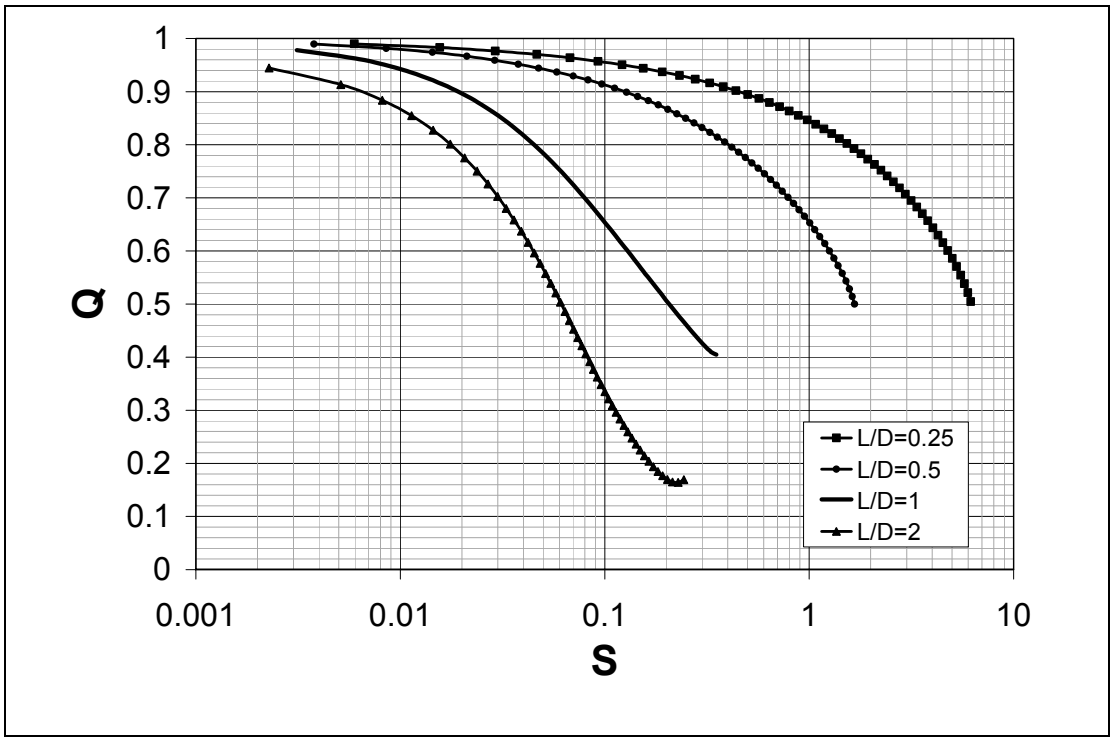

(b.)

Figure 32- Comparison of Raimondi and Boyd graphs for leakage rate, Q, vs. Sommerfeld number (a.) bearings without slip (b.) bearings with slip

In Figure 33, Figure 34 and Figure 35 a closer look is taken into how slip modifies bearing behavior. A single length to width ratio of 1 is chosen and the curves with and without slip (A=100 and A=0 respectively) are superimposed on the graphs.

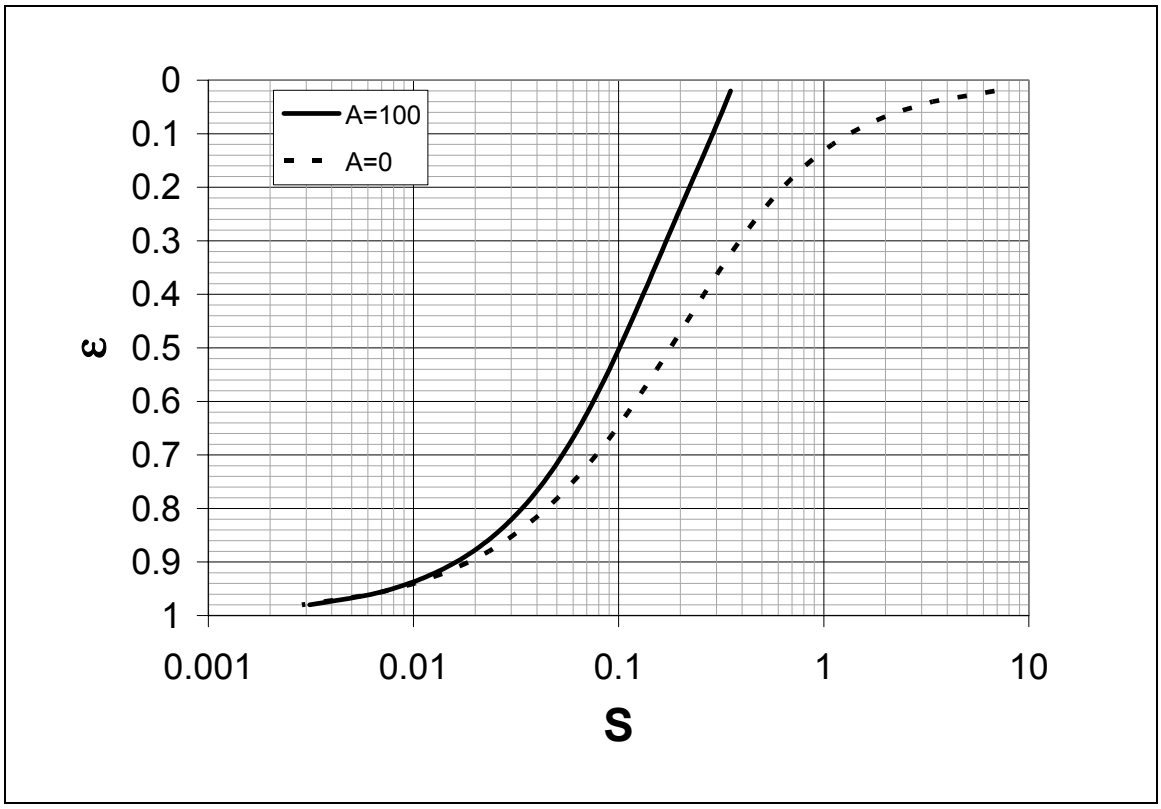

Figure 33- Eccentricity ratio vs. Sommerfeld number for bearing with A=100 and bearing with A=0, L/D=1

Figure 33 shows the effect of slip on the relationship between Sommerfeld number and eccentricity ratio. In general, the bearing with slip can sustain a higher load given the same eccentricity. The advantage, however, diminishes as the eccentricity becomes larger. Once it reaches a value over ε=0.92 the two bearings are essentially the same.

Another feature unique to the journal bearing with slip is that it can sustain a load at zero eccentricity. The Sommerfeld number attains a finite value at $\varepsilon=0$ as apposed to the asymptotic behavior of the no-slip bearing. This result is similar to that found for the plane pad bearing with high load support when the surfaces were parallel.

In Figure 34 the effect on friction coefficient is shown. The bearing with slip consistently maintains a lower friction coefficient for the same Sommerfeld number. Once again, the advantage is seen to diminish as the Sommerfeld number gets smaller.

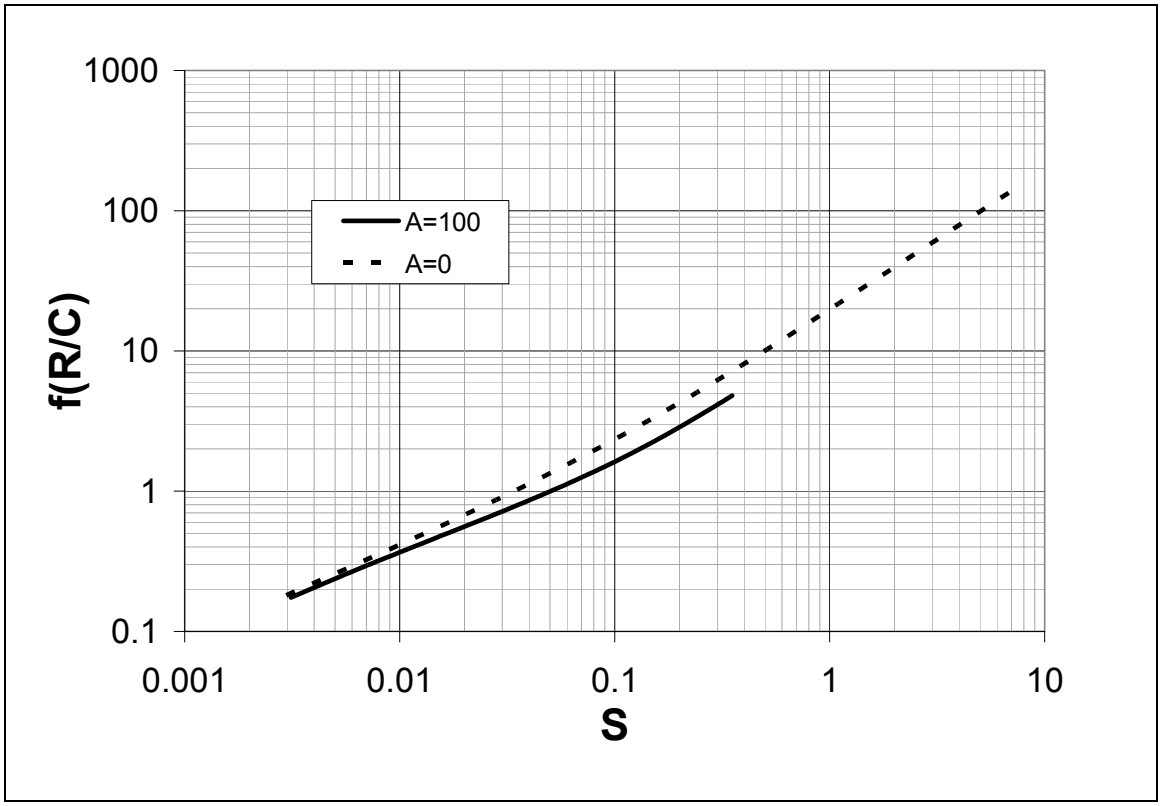

Figure 34- friction coefficient vs. Sommerfeld number for bearing with A=100 and bearing with A=0, L/D=1

Figure 35 is a graph of side leakage rate as function of Sommerfeld number. The side leakage rate for the bearing with slip falls below that of the bearing without slip. In order to interpret this result it is important to keep in mind that the side leakage rate in this graph is non-dimensionalized by the flow rate in the circumferential direction of the bearing.

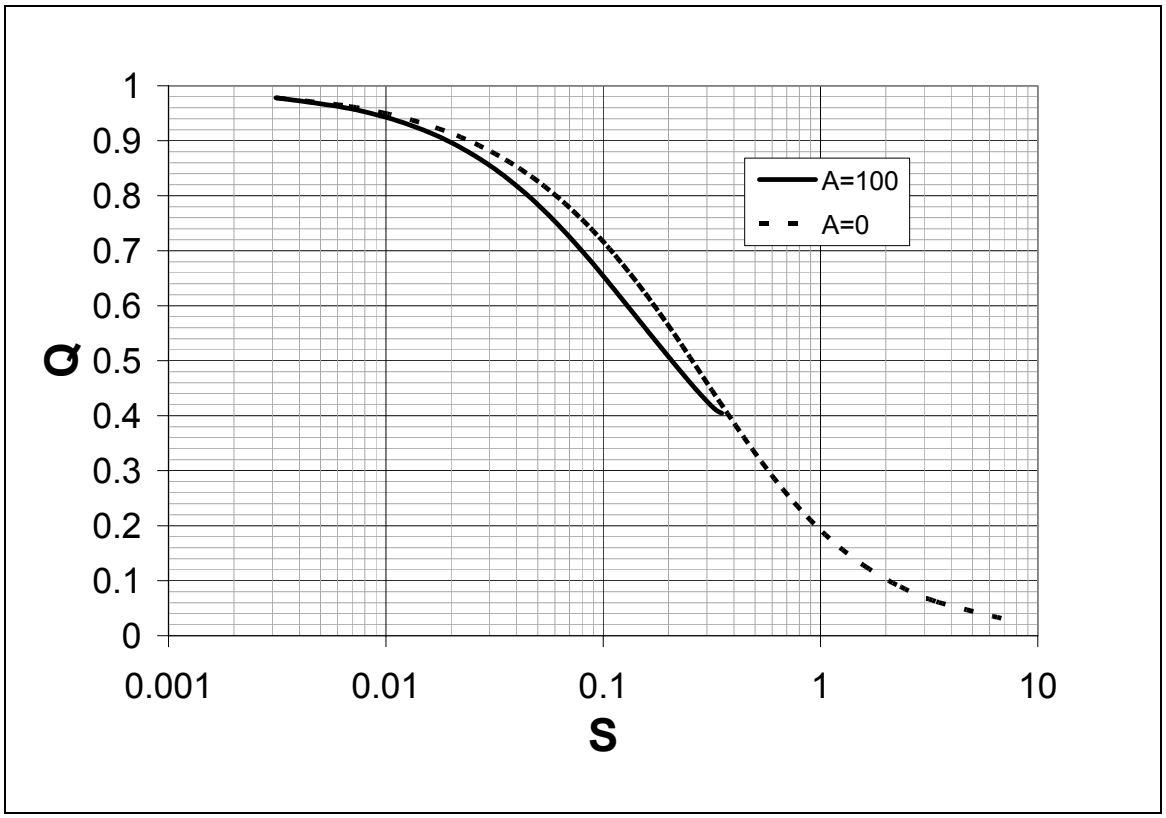

Figure 35- Leakage rate, Q, vs. Sommerfeld number for bearing with A=100 and bearing with A=0, L/D=1

In Figure 36 the alternate dimensionless flow rate, Q_y, is graphed as a function of Sommerfeld number. This result is more consistent with what was found in the case of the plane pad bearing. Q_y is greater for the bearing with slip than without.

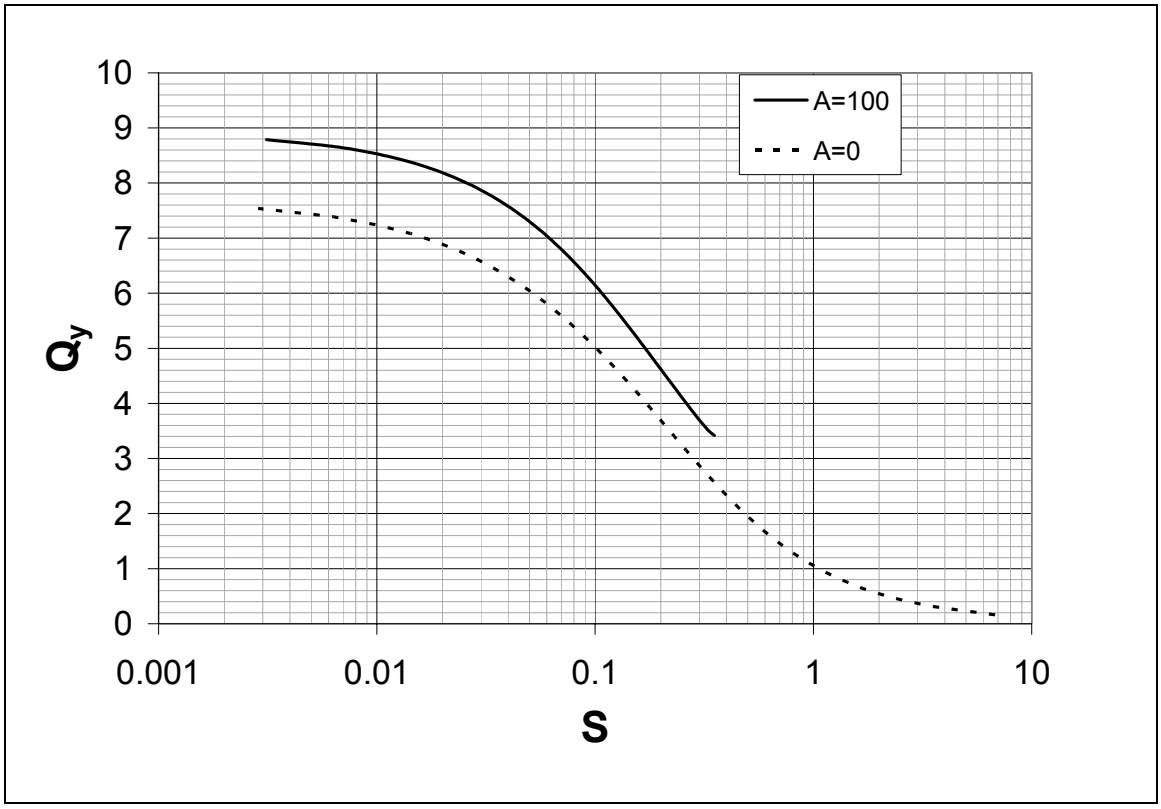

Figure 36- Leakage rate, Q_y, vs. Sommerfeld number for bearing with A=100 and bearing with A=0, L/D=1

The difference between the behaviors of Q and Q_y may be due to the difference in film thickness. As was seen in Figure 33, for the same load the journal bearing with slip sustains a lower eccentricity or a larger film thickness.

4.3 Case III – Slider Bearing with Critical Shear Stress Condition

The model for Case III was dominated by convergence problems. A hypothesis was made about how this case would behave. At low driving speeds the surface shear stress would not exceed the critical value at any location in the permissible slip region, resulting in a conventional no-slip bearing. As the speed increased nucleation of stable slip areas within the slip pad was expected. These areas were then expected to grow with increasing speed until the full pad experienced slip.

The actual results from the numerical simulation did conform to the hypothesis for both low and high speeds. At very low speeds the bearing did model as a fully no slip bearing. At high speeds the full slip pad was active. The load carrying capacities that resulted from bearings at these speeds were very close to the values found for the Navier Slip cases. For example, at a critical shear stress value of T=0.2 the solutions first converges to the full slip solution at a speed, U=88. At this point the load carrying capacities for the Navier slip condition and the critical shear stress condition differ by 1.1%. The leakage rates, Qy, differ by 1.8%. For both parameters the bearing with the critical shear stress gives the lower value. The difference between friction force for the critical shear stress case increases with increasing speed. At a U of 500 the percent difference is 4.6% with the critical shear stress case generating the lower friction force. .

For intermediate values of speed the program failed to converge. At this point it is unclear whether the phenomenon is a function of the program or the true physics of the system. One possibility would be that unsteady behavior occurs at these speeds which

are not captured with this steady state model. A full stability analysis is suggested for answering this question. Figure 37 shows a map of program convergence given as a function of the driving speed and critical shear stress value.

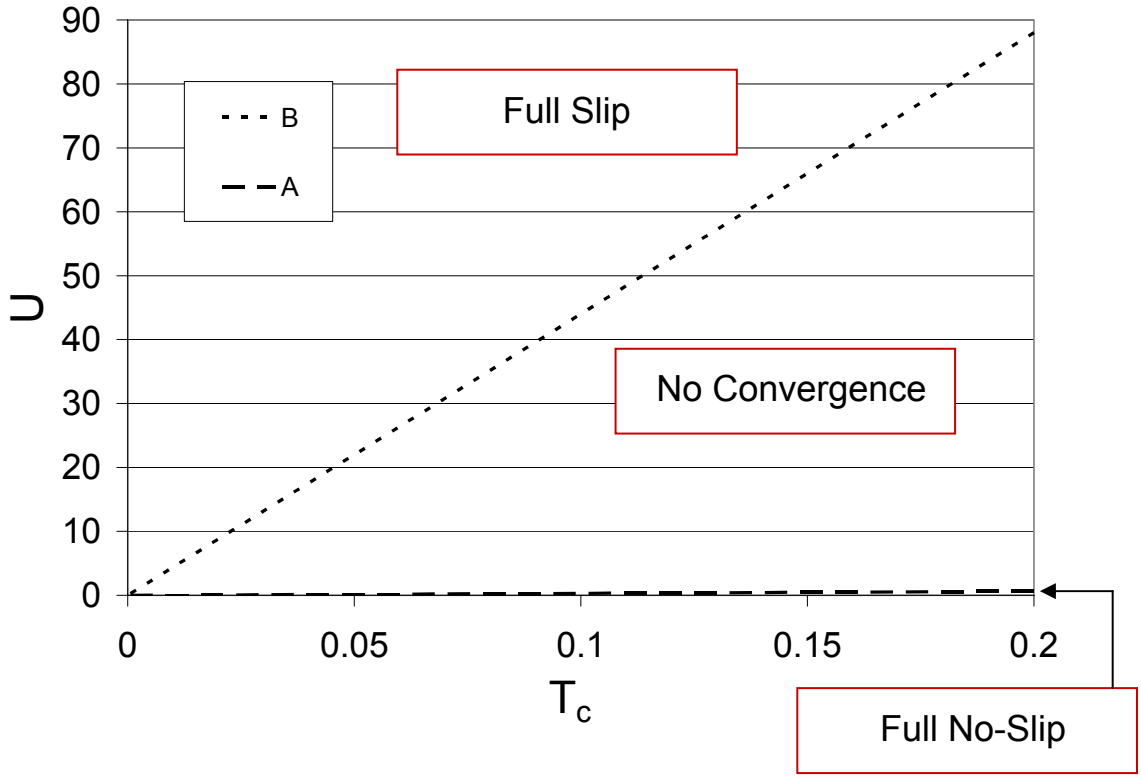

Figure 37- Graph of program convergence for Case III.

CHAPTER 5

CONCLUSION

This research project examined the benefit of a well chosen slip/ no-slip surface pattern on hydrodynamic bearing performance. Both plane pad and journal bearings were considered.

For the plane pad bearing it was found that the addition of slip can result in a significantly higher load carrying capacity and reduced friction forces. This was true for the geometric optimization cases as well as for the parametric analysis.

The representative plane pad bearing with slip produced as much as 2.5 times the load carrying capacity as the bearing without slip. The benefits were found to decrease with steeper inclines of Surface 2 as well as increasing recess depth. The contribution of changing slip coefficient was found to plateau after a value, A=10 was reached.

The results for friction force in the plane pad bearings with slip were as much as 0.67 times as large as those for bearings without slip. As with the load carrying capacity, the advantage diminished with increasing incline and recess depth.

The pressure profile produced for a bearing with slip mimics that produced by a bearing with recess suggesting that the mechanism by which they enhance pressure generation is the same. More investigation needs to be done into the effect slip has at very high recess depths.

Another area in which further research is recommended is the critical shear stress criteria. Results for the critical shear stress case were attained at very low speeds where no slip occurred and very high speeds where the full slip pad was active. At high speeds the bearing behavior was closely predicted by the results found for the Navier boundary condition with no critical shear stress, suggesting that the contribution of the critical shear stress was minimal at these high speeds. There was a large range of driving velocities, between the two convergent regions, over which no steady solution was attained. A stability analysis could determine the reason for such a result.

The results for the journal bearing working under Navier slip suggested an advantage over a conventional bearing in terms of both load carrying capacity and friction force for low and moderate eccentricities. At eccentricities above 0.92, however, little difference from a conventional bearing was found in the performance parameters.

REFERENCES

Baudry, J., E. Charlaix. 2001. "Experimental Evidence for a Large Slip Effect at a Nonwetting Fluid-Solid Interface." Langmuir 17: 5232-5236.

Goldstien, S., et al., eds. 1943. Modern Developments in Fluid Dynamics, Vol. 2. Oxford: University Press 676-680.

Hamrock, Bernard J. 1994. Fundamentals of Fluid Film Lubrication. New York: McGraw-Hill, Inc.: 157, 188.

Hasegawa, Masato, et al. 1999. "Drag Reduction on Microscale Concave-Convex Surface." Proceedings of the ASME Heat Transfer Division 364-1: 317-322

Horn, Roger G., et al. 2000. "Hydrodynamic Slippage Inferred from Thin Film Drainage Measurements in a Solution of Nonadsorbing Polymer." Journal of Chemical Physics 112.14: 6424

Meyer, E., et al. 1998. Nanoscience: Friction and Rheology on the Nanometer Scale. Singapore: World Scientific.

Migler, K.B., H. Hervet, and L. Leger. 1993. "Slip Transition of a Polymer Melt under Shear Stress." Physical Review Letters 70.3: 287-290.

Patankar, Suhas V. 1980. Numerical Heat Transfer and Fluid Flow. Washington: Hemisphere Publishing Corporation : 30-36,44-45,52-53.

Payvar, P., R. F. Salant. 1992. "A Computational Method for Cavitation in a Wavy Mechanical Seal." Journal of Tribology 114: 199-204.

Pit, R., H. Hervet, and L. Leger. 2000. "Direct Experimental Evidence of Slip in Hexadecane: Solid Interfaces." Physical Review Letters 80.5: 980-983.

Reiter, Gunter, et al. 1994. "Stick to Slip Transition and Adhesion of Lubricated Surfaces in Moving Contact." J. Chem. Phys. 101 (1994): 2606-2615.

Riedo, Elisa, Francis Levy, and Harald Brune. 2002. "Kinetics of Capillary Condensation in Nanoscopic Sliding Friction." Physical Review Letters 88.18: 185505 1-4.

Salant, R.F., A.E. Fortier. 2004. "Numerical Simulation of a Slider Bearing with an Engineered Slip/No-Slip Surface." Tribology and Lubrication Engineering: 14th International Colloquium Tribology. 13-15 Jan. Esslingen, Germany: Technische Akademie Esslingen : 1699-1704.

Spikes, Hugh, Steve Granick. 2003. "Equation for Slip of Simple Liquids at Smooth Solid Surfaces." Langmuir 19: 5065-5071.

Spikes, Hugh A. 2003a. "The Half-Wetted Bearing. Part 1: extended Reynolds equation." Proc. Inst. Mech. Eng., Part J 217: 1-14.

Spikes, Hugh A. 2003b. "The Half-Wetted Bearing. Part 2: Potential Application in Low Load Contacts." Proc. Inst. Mech. Eng., Part J 217: 15-26.

Watanabe, Keizo, Yanuar and Hiroshi Udagawa. 1999. "Drag Reduction of Newtonian Fluid in a Circular Pipe with a Highly Water-Repellent Wall." J. Fluid Mech. 381: 225-238.

Williams, J.A. 1994. Engineering Tribology. New York: Oxford University Press Inc.: 242.

Zhu, Yingxi, Steve Granick. 2001. "Rate Dependent Slip of Newtonian Liquids at Smooth Surfaces." Physical Review Letters 87.9: 096105 1-4.